Title

Peripherally derived angiotensin converting enzyme-enhanced macrophages alleviate Alzheimer-related disease.

Journal

Brain, 143(1)

ISSN

0006-8950

Authors

Koronyo-Hamaoui, Maya
Sheyn, Julia
Hayden, Eric Y
et al.

Publication Date

2020

DOI

10.1093/brain/awz364

Peer reviewed

doi:10.1093/brain/awz364 BRAIN 2020: 143; 336–358 | 336

BRAIN
A JOURNAL OF NEUROLOGY

Peripherally derived angiotensin converting enzyme-enhanced macrophages alleviate Alzheimer-related disease

Maya Koronyo-Hamaoui,[1,2] Julia Sheyn,[1] Eric Y. Hayden,[3] Songlin Li,[1,4] Dieu-Trang Fuchs,[1] Giovanna C. Regis,[1] Dahabada H.J. Lopes,[1] Keith L. Black,[1] Kenneth E. Bernstein,[2] David B. Teplow,[3] Sebastien Fuchs,[5] Yosef Koronyo[1,*] and Altan Rentsendorj[1,*]

*These authors contributed equally to this work.

Targeted overexpression of angiotensin-converting enzyme (ACE), an amyloid-β protein degrading enzyme, to brain resident microglia and peripheral myelomonocytes (ACE^{10} model) substantially diminished Alzheimer's-like disease in double-transgenic $APP_{SWE}/PS1_{\Delta E9}$ (AD^+) mice. In this study, we explored the impact of selective and transient angiotensin-converting enzyme overexpression on macrophage behaviour and the relative contribution of bone marrow-derived ACE^{10} macrophages, but not microglia, in attenuating disease progression. To this end, two *in vivo* approaches were applied in AD^+ mice: (i) $ACE^{10/GFP+}$ bone marrow transplantation with head shielding; and (ii) adoptive transfer of $CD115^+$-$ACE^{10/GFP+}$ monocytes to the peripheral blood. Extensive *in vitro* studies were further undertaken to establish the unique ACE^{10}-macrophage phenotype(s) in response to amyloid-β_{1-42} fibrils and oligomers. The combined *in vivo* approaches showed that increased cerebral infiltration of ACE^{10} as compared to wild-type monocytes (~3-fold increase; $P < 0.05$) led to reductions in cerebral soluble amyloid-β_{1-42}, vascular and parenchymal amyloid-β deposits, and astrocytosis (31%, 47–80%, and 33%, respectively; $P < 0.05$–0.0001). ACE^{10} macrophages surrounded brain and retinal amyloid-β plaques and expressed 3.2-fold higher insulin-like growth factor-1 ($P < 0.01$) and ~60% lower tumour necrosis factor-α ($P < 0.05$). Importantly, blood enrichment with $CD115^+$-ACE^{10} monocytes in symptomatic AD^+ mice resulted in pronounced synaptic and cognitive preservation ($P < 0.05$–0.001). *In vitro* analysis of macrophage response to well-defined amyloid-β_{1-42} conformers (fibrils, prion rod-like structures, and stabilized soluble oligomers) revealed extensive resistance to amyloid-β_{1-42} species by ACE^{10} macrophages. They exhibited 2–5-fold increased surface binding to amyloid-β conformers as well as substantially more effective amyloid-β_{1-42} uptake, at least 8-fold higher than those of wild-type macrophages ($P < 0.0001$), which were associated with enhanced expression of surface scavenger receptors (i.e. CD36, scavenger receptor class A member 1, triggering receptor expressed on myeloid cells 2, CD163; $P < 0.05$–0.0001), endosomal processing ($P < 0.05$–0.0001), and ~80% increased extracellular degradation of amyloid-β_{1-42} ($P < 0.001$). Beneficial ACE^{10} phenotype was reversed by the angiotensin-converting enzyme inhibitor (lisinopril) and thus was dependent on angiotensin-converting enzyme catalytic activity. Further, ACE^{10} macrophages presented distinct anti-inflammatory (low inducible nitric oxide synthase and lower tumour necrosis factor-α), pro-healing immune profiles (high insulin-like growth factor-1, elongated cell morphology), even following exposure to Alzheimer's-related amyloid-β_{1-42} oligomers. Overall, we provide the first evidence for therapeutic roles of angiotensin-converting enzyme-overexpressing macrophages in preserving synapses and cognition, attenuating neuropathology and neuroinflammation, and enhancing resistance to defined pathognomonic amyloid-β forms.

1 Department of Neurosurgery, Maxine Dunitz Neurosurgical Institute, Cedars-Sinai Medical Center, Los Angeles, CA 90048, USA
2 Department of Biomedical Sciences, Cedars-Sinai Medical Center, Los Angeles, CA 90048, USA
3 Department of Neurology, David Geffen School of Medicine at UCLA, Mary S. Easton Center for Alzheimer's Disease Research at UCLA, Brain Research Institute, Molecular Biology Institute, University of California, Los Angeles, CA 90095, USA

Received April 11, 2019. Revised September 17, 2019. Accepted October 1, 2019. Advance Access publication December 3, 2019

4 Institute of Neuroscience and Chemistry, and Institute of Life Sciences, Wenzhou University, Wenzhou, Zhejiang, China
5 College of Osteopathic Medicine of the Pacific, Western University of Health Sciences, Pomona, CA 91766, USA

Correspondence to: Maya Koronyo-Hamaoui
Departments of Neurosurgery and Biomedical Sciences, Cedars-Sinai Medical Center,
127 S. San Vicente Blvd., Los Angeles, CA 90048 Los Angeles, CA 90048, USA
E-mail: maya.koronyo@csmc.edu

Keywords: IGF1; TNFα; TREM2; EEA1; innate immunity

Abbreviations: AD^+ = $APP_{SWE}/PS1_{\Delta E9}$ double transgenic; BM = bone marrow; CAA = cerebral amyloid angiopathy; ICC = immunocytochemistry; IHC = immunohistochemistry; MΦ = macrophages; MSD = Meso Scale Discovery; Scara1 = scavenger receptor A; WT = wild-type

Introduction

Neuroinflammation is a key feature of Alzheimer's disease, a relentless, progressive, and currently untreatable neurodegenerative disease and the leading cause of senile dementia worldwide (Wyss-Coray, 2006; Gjoneska *et al.*, 2015; Heneka *et al.*, 2015; Alzheimer's Association, 2019). In Alzheimer's disease, the detrimental or therapeutic contribution of peripherally derived monocytes, compared to that of brain-resident microglia, is highly debated (Simard *et al.*, 2006; Ajami *et al.*, 2007; Butovsky *et al.*, 2007; El Khoury *et al.*, 2007; Mildner *et al.*, 2007; Koronyo-Hamaoui *et al.*, 2009; Lebson *et al.*, 2010; Bernstein *et al.*, 2014*b*; Jay *et al.*, 2015*a*, *b*; Koronyo *et al.*, 2015; Zuroff *et al.*, 2017; Cao and Zheng, 2018; Cronk *et al.*, 2018; Da Mesquita *et al.*, 2018). Several studies have demonstrated that monocytes can colonize diseased brain parenchyma in murine models of Alzheimer's disease (Simard *et al.*, 2006; Butovsky *et al.*, 2007; Cronk *et al.*, 2018) as well as under irradiation-free physiological conditions (Koronyo-Hamaoui *et al.*, 2009; Lebson *et al.*, 2010; Michaud *et al.*, 2013; Bernstein *et al.*, 2014*b*; Koronyo *et al.*, 2015; Rentsendorj *et al.*, 2018). In addition, heterogeneous subpopulations of brain resident microglia have been identified as having molecular signatures that are distinct from those of peripheral monocytes, particularly disease-associated microglia located proximal to the Alzheimer's disease pathological hallmark, amyloid-β plaques (Keren-Shaul *et al.*, 2017; Krasemann *et al.*, 2017; Yin *et al.*, 2017). These microglial populations play a role in the pathogenesis of chronic inflammation (Akiyama *et al.*, 2000; Bales *et al.*, 2000; Colton *et al.*, 2000; McGeer and McGeer, 2002; Wyss-Coray, 2006; Prinz *et al.*, 2011) and synaptic loss by excessive pruning (Hong *et al.*, 2016; Johnson and Stevens, 2018), while insufficiently clearing misfolded amyloid-β (Morgan *et al.*, 2005; Simard *et al.*, 2006; El Khoury *et al.*, 2007; Hickman *et al.*, 2008; Koronyo-Hamaoui et al., 2009; Yamanaka *et al.*, 2012; Frenkel *et al.*, 2013; Roussos *et al.*, 2015). In contrast, peripherally recruited monocytes and macrophages in Alzheimer's disease model mice were shown to exhibit a neuroprotective phenotype, regulating neuroinflammation and effectively eliminating cerebral amyloid-β pathology (Butovsky *et al.*, 2007; Koronyo-Hamaoui *et al.*, 2009; Bernstein *et al.*, 2014*b*; Koronyo *et al.*, 2015; Rentsendorj *et al.*, 2018). These beneficial effects provide the rationale for a comprehensive assessment of the therapeutic potential of peripheral monocyte infusion in animal models and eventually in Alzheimer's disease patients.

The pathology of Alzheimer's disease occurs as a complex continuum, typically characterized by early accumulation and aggregation of cerebral amyloid-β (Masters *et al.*, 2015; Jack *et al.*, 2018) in the form of parenchymal plaques and vascular deposits (e.g. cerebral amyloid angiopathy, CAA) (Ellis *et al.*, 1996), which extend to the neurosensory retina in patients with Alzheimer's disease (Koronyo-Hamaoui *et al.*, 2011; La Morgia *et al.*, 2016; Koronyo, 2017). The 42 amino acid-long form of amyloid-β has been regarded as pathognomonic to Alzheimer's disease, particularly its oligomeric forms, which display high synaptotoxicity, disrupt long-term potentiation, and directly induce cognitive impairments (Selkoe, 2008; Shankar *et al.*, 2008; Hayden and Teplow, 2012). At the same time, the precise structural characterization and impact of various amyloid-β_{42} species on cells have been challenging to investigate because of their highly metastable nature and their existence in dynamically changing mixtures (Walsh and Selkoe, 2004; Glabe, 2005; Kirkitadze and Kowalska, 2005). To this end, methods have been developed to chemically stabilize the different assembly types of amyloid-β_{42} such that a well-defined population of oligomers can be studied (Bitan *et al.*, 2003; Bitan and Teplow, 2004; Hayden and Teplow, 2012; Lopes *et al.*, 2012) in comparison with other naturally stable structures, including prion rod-like enriched assemblies and fibrils (Walsh *et al.*, 1997). It is widely believed that approaches to target and remove soluble amyloid-β_{42} oligomers from CNS tissues hold great promise for curbing neuroinflammation and contributing to Alzheimer's disease prevention and therapy (Haass and Selkoe, 2007; Viola and Klein, 2015).

In the past decade, strategies harnessing peripheral innate immune cells such as monocytes and macrophages were effective in clearing parenchymal and vascular amyloid-β in the brain and attenuating progression in mouse models of Alzheimer's disease (Malm *et al.*, 2005; Butovsky *et al.*, 2007; Town *et al.*, 2008; Boissonneault *et al.*, 2009;

Koronyo-Hamaoui *et al.*, 2009; Lebson *et al.*, 2010; Michaud *et al.*, 2013; Bernstein *et al.*, 2014*b*; Koronyo *et al.*, 2015; Ardura-Fabregat *et al.*, 2017; Rentsendorj *et al.*, 2018). Importantly, even in the absence of whole-body irradiation or microglial ablation via pharmacological intervention, peripheral monocytes spontaneously engrafted into the brain of transgenic $APP_{swe}/PS1_{\Delta E9}$ (AD^+) mice and homed to amyloid-β plaque sites (Lebson *et al.*, 2010; Koronyo *et al.*, 2015). In particular, enhanced recruitment of cerebral amyloid-β-associated monocytes was achieved through blood enrichment with bone marrow (BM)-derived $CD115^+$ monocyte subsets isolated from young donor mice, leading to diminished neuropathology and preserved cognitive function (Koronyo *et al.*, 2015). To augment these beneficial immune responses further, our group studied a mouse model of Alzheimer's disease in which the animals were genetically modified to overexpress angiotensin-converting enzyme (ACE), an amyloid-β-degrading peptidase, controlled by a c-fms promoter (Bernstein *et al.*, 2014*b*).

The role of ACE and ACE inhibitors in Alzheimer's disease is complex (Kehoe *et al.*, 2009). In humans, a recent large genome-wide association meta-analysis (GWAS) of 94 437 individuals clinically diagnosed with late-onset Alzheimer's disease has corroborated previous studies and identified *ACE* as a candidate gene (Kunkle *et al.*, 2019). In addition, GWAS-by-familial-proxy of Alzheimer's or dementia studies have further confirmed ACE relevance to Alzheimer's disease and identified the single nucleotide polymorphism (SNP) combination of rs4343 and rs4351 in the ACE haplotype to possess a 45-fold increased risk of developing Alzheimer's disease (Meng *et al.*, 2006; Marioni *et al.*, 2018). Importantly, individuals carrying variants of the *ACE* gene (D/D alleles) resulting in increased plasma expression of the enzyme were associated with lower risk for Alzheimer's disease (Kehoe *et al.*, 1999; Lehmann *et al.*, 2005). Lower CSF levels of ACE and higher brain ACE were also detected in Alzheimer's disease patients (Miners *et al.*, 2008, 2009).

In our previous studies in mice, ACE was selectively expressed in myelomonocytic cells such as monocytes, macrophages, and microglia (Bernstein *et al.*, 2014*a*, *b*). The rationale for this experiment was 2-fold: myeloid cell ACE overexpression markedly enhances innate immune responses (Shen *et al.*, 2007; Koronyo-Hamaoui *et al.*, 2014; Bernstein *et al.*, 2018), and surface expression of ACE would promote amyloid-β_{42} cleavage and conversion into shorter, more benign amyloid-β alloforms via ACE enzymatic activity (Hemming and Selkoe, 2005; Bernstein *et al.*, 2014*b*). In fact, AD^+ mice overexpressing ACE in myelomonocytes displayed minimal to no Alzheimer's disease-like phenotype (Bernstein *et al.*, 2014*b*). However, in those experiments, ACE overexpression was present throughout the life of the AD^+ mice in both macrophages and microglia due to an inserted genetic modification in the ACE gene. Hence, the relative therapeutic contribution of a periodic addition of peripherally derived ACE-overexpressing monocytes and macrophages, as opposed to brain-resident microglia, has yet to be investigated.

Here, we examine whether exogenous administration of bone marrow-derived $CD115^+$ myeloid cells overexpressing ACE, either by bone marrow transplantation or by peripheral blood enrichment, can also reduce the magnitude of disease. The use of bone marrow-derived myeloid cells isolated from green fluorescent protein (GFP) mice allowed unambiguous tracing of the grafted cells' destiny in the CNS of recipient animals; this was especially critical to distinguish clearly between the contribution of microglia and macrophages to the phenotype. Moreover, our experiments showed that ACE^{10} monocytes and macrophages were highly potent in clearing soluble and insoluble forms of amyloid-β_{42}, as well as in reducing neuropathology and preserving synapses and cognitive function in murine Alzheimer's disease models.

Materials and methods

Mice used in the experiments

The mice selected to be recipients of bone marrow transplantation or adoptive transfer of monocytes were from the double-transgenic B6.Cg-Tg $(APP_{SWE}/PS1_{\Delta E9})$85Dbo/Mmjax hemizygous ($AD^+$) mice strain (MMRRC stock #34832-JAX|APP/PS1) and their non-transgenic littermates (as wild-type control non-Alzheimer's disease). These animals were purchased from Jackson Laboratories and later bred and maintained at Cedars-Sinai Medical Center. For the bone marrow transplantation experiment, we used 22 AD^+ recipient mice divided into three groups as follows: BM^{AD+}::AD^+ (n = 7, four females and five males), BM^{WT}::AD^+ (n = 7, two females and five males), and BM^{ACE10}::AD^+ (n = 8, three females and five males). For adoptive transfer experiments we used 30 mice, all males, divided into four groups as follows: AD^+ recipients of either wild-type monocytes (Mo^{WT}) (n = 8) or Mo^{ACE10} (n = 8), PBS-injected AD^+ controls (n = 7), and non-transgenic naïve wild-type mice (n = 7).

The $ACE^{10/10}$ donor mice strain overexpresses ACE (two alleles) in the myelomonocytic cell lineage (Supplementary Fig. 1A and B) (Bernstein *et al.*, 2014*b*). The *Ace* genotypes used in this study were wild-type (ACE^{WT}; n = 30) and homozygous for the targeted allele (ACE^{10}; n = 30). The GFP donor mice were B6-TgN (β-act-EGFP) osbY01 (Okabe *et al.*, 1997; Okwan-Duodu *et al.*, 2010), which had been backcrossed at least 10 generations to a C57BL/6 background (Jackson Laboratory; n = 15). This line has enhanced GFP (EGFP) cDNA under the control of a chicken β-actin promoter and a cytomegalovirus enhancer. These animals are also available at Jackson Laboratory [C57BL/6-Tg(CAG-EGFP)10sb/J; #003291].

The bone marrow donor mice strains (ACE^{10} and GFP) were crossed to produce the genotypes $GFP^+AD^-ACE^{WT}$ (n = 76 mice), $GFP^+AD^-ACE^{10}$ (n = 85), and $GFP^-AD^+ACE^{WT}$ (n = 4 mice) used for the *in vivo* experiments. Bone marrow transplantation donor mice were 12–16 weeks old (n = 11, all females). Adoptive transfer donor mice were used at the age of 8–12 weeks old (n = 154, female and males at equal

numbers). All mice used for these experiments were on the genetic background of B6. All experiments were conducted in accordance with Cedars-Sinai Medical Center Institutional Animal Care and Use Committee (IACUC) guidelines under an approved protocol.

Bone marrow transplantation

With their heads shielded, 2-month-old recipient AD^+ mice were subjected to 9.5 Gy (950 rad) irradiation for 11 min—a dose lethal to proliferating cells. The cells were immediately reconstituted by intravenous administration of 5×10^6 donor marrow cells [isolated from 2-month-old GFP-expressing donor mice (described above)]. As irradiation of the brain significantly increases infiltration of immune cells, we protected the mice brains from irradiation with an extensive lead-shielding device that we had constructed (Supplementary Fig. 1C). After 8 weeks of bone marrow repopulation, engraftment was assessed by flow cytometry analysis of peripheral blood for GFP expression. Non-invasive retinal imaging was carried out when the mice reached 7 months of age. When they were 8 months old, the recipient mice were anaesthetized and perfused with 0.9% ice-cold saline containing 0.5 mM EDTA. Brain, eyes, and blood were collected. Retinal flatmounts were immediately isolated and fixed in 2.5% paraformaldehyde (PFA) as previously described (Koronyo-Hamaoui *et al.*, 2011). One brain hemisphere was fixed for histology in 2.5% PFA containing 30% sucrose and the other hemisphere was snap-frozen for further analysis.

Monocyte adoptive transfer

After the animals had been euthanized, bone marrow cells were harvested and enriched for mononuclear cells on a Ficoll density gradient as previously described (Koronyo *et al.*, 2015). Five to six million $CD115^+$-Mo^{BM} cells were injected intravenously into each AD^+ recipient mouse, beginning when the animal was 8 months old and continuing once a month for 3 months to ensure long-term elevated levels of transfused monocytes. Animals in the control group received intravenous injections of phosphate-buffered saline (PBS). Characterization of isolated monocytes was performed by flow cytometry. After completion of behavioural testing at 11 months old, the recipient mice were perfused, as described above, to collect tissues for analysis.

Non-invasive retinal imaging

After deep anaesthesia had been induced in the animals, the mouse pupils were dilated with 0.5% phenylephrine hydrochloride ophthalmic solution (Bausch and Lomb) combined with 0.5% tropicamide ophthalmic solution (Mydral, Bausch and Lomb). The retinas were imaged *in vivo* using the Micron III microscope with predetermined light exposure time and intensity, using identical gain and shutter modes for all animals as previously described (Koronyo-Hamaoui *et al.*, 2011; Koronyo *et al.*, 2012, 2017). Images and videos of the retina were repeatedly captured at several angles to visualize a larger retinal field and eliminate non-specific reflection signals. Images were exported to ImageJ 1.46r for analysis.

Behavioural tests

To assess locomotor activity and cognitive functions of the treated mice, we performed open field and Barnes maze tests, as previously described (Koronyo *et al.*, 2015). In the open field test, each mouse was placed in an individual apparatus for 60 min to record ambulatory and rearing activity. In the Barnes maze test, the mice were first trained for 4 days (acquisition-training phase), three times per day for 240 s for each trial per mouse. Following a 2-day break, the mice were retested for memory retention (retention phase, Day 7) and then short-term memory (reversal phase on Days 8 and 9) under the same conditions. Latency times and incorrect entries (errors) were recorded manually and by using a video camera (Koronyo *et al.*, 2015).

Immunohistochemistry

Coronal brain sections (30 μm) and retinal flatmounts were treated for 30 min in antigen-retrieval solution (Dako S1699) prior to serum-free protein blocking (Dako X0909). Tissues were then hybridized with various primary antibodies (Table 1) overnight at 4°C. Hybridization with primary antibodies was followed by incubation with fluorophore-conjugated secondary antibodies (1 h at 37°C) (Table 1). Stained tissues were mounted using ProLong® Gold with DAPI (Molecular Probes, Life Technologies). Negative controls were processed using the same protocol with the omission of the primary antibody to assess non-specific labelling.

Thioflavin-S staining

For amyloid burden assessment in brain parenchyma and vasculature, sections were stained with Thioflavin S (Thio-S, 1% w/v in 70% ethanol; Sigma-Aldrich) for 10 min at room temperature, following the secondary antibody step, washed three times in 70% ethanol for 1 min each, then rinsed in distilled water before mounting.

Curcumin staining

Curcumin (diferuloylmethane; $C_{21}H_{20}O_6$; Sigma-Aldrich) was dissolved in 0.5 M NaOH followed by immediate dilution in PBS to a final solution of 0.1 mg/ml curcumin (pH 7.9). Brain sections were stained with curcumin solution for 10 min at room temperature, and then rinsed three times with PBS for 5 min each, as previously reported (Koronyo-Hamaoui *et al.*, 2009).

Cerebral amyloid angiopathy scoring

Severity scores for the degree of CAA were defined by inspection of Thio-S-labelled brain sections using a scale of 0–4 (0 = no CAA, 1 = low, 2 = medium, 3 = high and 4 = severe CAA) (Wyss-Coray *et al.*, 2001; Rentsendorj *et al.*, 2018). Eighteen images encompassing three to four brain sections and covering both cortex (n = 9 images) and hippocampus (n = 9) were analysed for each animal (total of n = 22 mice, n = 6–9 per experimental group).

Table 1 List of antibodies used in the study

	Antigen	Source species	Dilution	Commercial source	Catalogue #
IHC, ICC	**Primary antibodies**				
	Arginase1 pAb	Rabbit	1:100	Santa Cruz	sc-20150
	Beclin1 pAb	Rabbit	1:100	Abcam	ab16998
	CD163 pAb	Rabbit	1:100	Biorbyt	Orb13303
	CD204 mAb Scavenger R Type I/II (SCARA-1)	Rat	1:100	AbD Serotec	MCA1322
	CD36 mAb clone MF3	Rat	1:200	Abcam	ab80080
	CD45 mAb clone 30-F11	Rat	1:25	BD Pharmingen	#550539
	EEA1 pAb	Rabbit	1:100	Millipore	07-1820
	GFAP mAb	Rat	1:100	Invitrogen	13-0300
	GFAP pAb	Rabbit	1:100	Sigma-Aldrich	G926
	GFP pAb	Rabbit	1:500	MBL	#598
	Human amyloid-β residues 17–24, mAb clone 4G8	Mouse	1:100	Covance/BioLegend	800711
	Human amyloid-β residues 1–16, mAb clone 6E10	Mouse	1:100	Covance/BioLegend	803003
	Iba1 pAb	Rabbit	1:200	Wako Chemicals USA	#019-19741
	IGF1 pAb	Goat	1:30	R&D systems	AF791
	iNOS mAb	Rabbit	1:400	Cell Signaling	13120
	Lamp1 mAb	Rat	1:500	Abcam	ab25245
	Lamp2 mAb, clone M3/84	Rat	1:500	Millipore	MABC24
	MMP9	Goat	1:100	R&D systems	AF909
	PSD95 mAb	Rabbit	1:600	Abcam	ab76115
	TREM2 pAb	Goat	1:100	Abcam	ab95470
	VGluT1 pAb	Guinea pig	1:6000	Millipore	AB5905
	Secondary antibodies				
	Cy2 (anti-mouse, rat, rabbit, goat IgG)	Donkey	1:200	Jackson ImmunoResearch Laboratories	
	Cy3 (anti-mouse, rat, rabbit, goat, guinea pig IgG)	Donkey	1:200	Jackson ImmunoResearch Laboratories	
	Cy5 (anti-mouse, rat, rabbit, goat IgG)	Donkey	1:200	Jackson ImmunoResearch Laboratories	
Flow cytometry	CD11b mAb clone M1/70 (PE/Cy7)	Rat	1 µl*	eBioscience/ThermoFisher	25-0112-81
	CD45 mAb clone 30-F11 (PE)	Rat	1 µl*	eBioscience/ThermoFisher	12-0451-81
	F4/80 mAb clone BM8 (FITC)	Rat	1 µl*	eBioscience/ThermoFisher	11-4801-81
	Human amyloid-β residues 1–16, mAb clone 6E10	Mouse	1:500	Covance/BioLegend	803003
	IL10 mAb clone JES5-16E3 (PerCP-Cy5.5)	Rat	1 µl*	BioLegend	505028
	Ly-6C mAb clone HK1.4 (eFluor450)	Rat	1 µl*	eBioscience/ThermoFisher	48-5932-80
	TGFβ mAb clone TW7-16B4 (PerCP-Cy5.5)	Mouse	1 µl*	BioLegend	141410
	TNFα mAb clone MP6-XT22 (APC)	Rat	1 µl*	BioLegend	506308

mAb = monoclonal antibody; pAb = polyclonal antibody.
*1 µl = 1 µl per 100 000 – 1 000 000 cells.

Primary culture of bone marrow-derived macrophages

Bone marrow was harvested from the femora and tibiae of wild-type or ACE^{10} mice donors after they had been euthanized at the age of 8–12 weeks (3–5 mice/genotype), as previously described (Rentsendorj *et al.*, 2018). Briefly, the cells were cultured for 7 days in RPMI supplemented with 10% foetal bovine serum (FBS), 100 U/ml antibiotic, 2 mM L-glutamine, and 20 ng/ml MCSF. On the sixth day, macrophages (MΦ) were plated overnight in 24-well tissue culture plates with or without glass coverslips (10^5 cells/well) depending on which analysis was planned [immunocytochemistry (ICC) or ELISA]. The following day, macrophages were either unstimulated (not treated with amyloid-β) or stimulated by one of the three amyloid-β_{42} alloforms (100 nM and 250 nM; fibril amyloid-β_{42}, prion rod-like amyloid-β_{42}, oligomer amyloid-β_{42}). $M\Phi^{ACE10}$ were analysed as compared to $M\Phi^{WT}$ for cell-surface amyloid-β_{42} binding; for this, the plates were chilled for 10 min on ice (0°C) followed by addition of amyloid-β_{42} and spun at 515 *g* for 1 min, followed by incubation for another 10 min at 0°C (binding – 0' time point). $M\Phi^{ACE10}$ were also analysed for receptor expression as well as uptake of amyloid-β_{42} forms at incremental time points from 5 min up to 60 min (incubated at 37°C; uptake –5, –15, –30 min). After each time point, media were collected for biochemical analysis (ELISA). The cells were rinsed with culture medium and then washed with PBS before being fixed in cold methanol (–20°C) for ICC. In parallel, another subset of $M\Phi^{ACE10}$ were treated overnight (in RPMI + 0.3% BSA) with lisinopril (1 µM) the day before

plating in 24-well plates and then exposed to 100 nM fibril amyloid-β_{42} for 0, 5, or 30 min.

Primary culture of peritoneal-derived macrophages

Peritoneal macrophages were collected from the peritoneum as described previously (Okwan-Duodu *et al.*, 2010). Briefly, the macrophages were harvested from the peritoneal cavity 4 days after a 2 ml intraperitoneal injection of 3% thioglycolate. The cells were cultured at 37°C, 5% CO_2 in RPMI 1640 medium enriched with 10% foetal calf serum, 50 µM 2-ME, 0.5 mM sodium pyruvate, 10 mM HEPES buffer, 50 units/ml penicillin, 50 µg/ml streptomycin, and 2 mM L-glutamine. For purification of the macrophages, peritoneal exudates were allowed to adhere for 2 h, after which non-adherent cells were removed with PBS to achieve >90% purity of macrophages.

Immunocytochemistry

Briefly, after serum-free protein blocking (Dako X0909), cells were hybridized with various primary antibodies (Table 1) overnight at 4°C. The following day, these cells were incubated with fluorophore-conjugated secondary antibodies (1 h at 37°C). Coverslips were mounted onto plates using ProLong® Gold with DAPI (Molecular Probes, Life Technologies).

Microscopy and quantification

A Karl Zeiss fluorescence microscope (Imager, Z1, ApoTome and MBF equipped) was used for microscopic analysis. For immunohistochemistry (IHC), three to six comparable coronal brain sections, originally located 150 µm apart, were used for quantitative analysis. For ICC, four to six samples were analysed. Numbers, area, and intensity of amyloid-β deposits, $GFAP^+$ and GFP^+ cells, were determined automatically by using NIH ImageJ software or an MBF stereological system. The same approach was used to analyse cytokines and other markers.

Image analysis

To cover the hippocampal area for synaptic analysis, 15 fields per hippocampal area per brain were taken under 100× oil objective lens and analysed (as previously described in Koronyo *et al.*, 2015). Single optical section images at 0.25 µm intervals and 3.75 µm Zeiss ApoTome high-resolution scans were performed. Synaptic immunoreactive area and co-localization of $EEA1^+$ with $6E10^+$ immunoreactive area were quantified using Puncta Analyzer as previously described (Ippolito, 2010) and ImageJ (NIH) macro and batch process.

To quantify co-localized $IGF1^+$ immunoreactive in monocytes (Mo)/MΦ ($Iba1^+CD45^{high}$ cells), images were first compiled and analysed in Adobe Photoshop (Adobe Systems Inc., Mountain View, CA, USA). The per cent of $IGF1^+$ foci were obtained by tracing an outline around each plaque associated with inflammation site. IGF1 (red) co-localizing with CD45 (green) was quantified by measuring the fluorescence of coincident (yellow) particles. Frequency of coincidence of $IGF1^+$ area co-localizing with Iba^+CD45^{high} cells in cortices was plotted as percentage (%) in BM^{WT}::AD^+ versus BM^{ACE10}::AD^+ chimeric mice (n = 4–7 AD^+ mice/group).

Elongation factor

The long and short axes of cells were manually measured in micrometres from microscopic images using length tools in the AxioVision Rel. 4.8 software package. At least 100 cells were examined in each experiment in which individual cells were assayed by microscopy.

Quantitative Meso Scale Discovery protein assay

The Meso Scale Discovery (MSD) V-PLEX proinflammatory Panel I (MSD K15048D-1) consists of highly sensitive multiplex ELISAs that quantitatively measure 10 cytokines (IFN-γ, IL-10, IL-12p70, IL-1β, IL-2, IL-4, IL-5, IL-6, KC/GRO or CXCL1, TNFα) using electrochemiluminescence detection technology.

Preparation of standards/calibrators and samples

The highest calibrator (Calibrator 1) was prepared by adding 1 ml of Diluent 41 to the lyophilized calibrator vial according to the manufacturer's protocol. Seven calibrator solutions were made by first transferring 100 µl of the highest calibrator into 300 µl of Diluent 41 and then making 4-fold serial dilutions five additional times. Diluent 41 was used for the zero calibrator. Sixty microlitres of each sample was mixed with 60 µl of Diluent 41 to achieve a 2-fold dilution of each sample.

Plate preparation

A 1× wash buffer was made by a 20-fold dilution of the stock (supplied in the kit) using deionized water. The plate was washed with 150 µl of wash buffer three times and tapped dry. Calibrators and samples (50 µl) were pipetted into the assigned wells. The plate was incubated for 2 h at room temperature on a shaker. To make 1× detection antibodies from 50× stock, 60 µl of each detection antibody for each analyte was pipetted into 2.4 ml of Diluent 45. After the 2 h incubation, the plate was washed three times with wash buffer and tapped dry. Each well received 25 µl of detection antibody solution, after which the plate was incubated at room temperature with shaking for 2 h. To read the plate on the MSD instrument (MESO Quicklex S 120), the plate was first washed with 150 µl wash buffer three times and tapped dry, then 150 µl of 2× Read Buffer (supplied in the kit) was pipetted into each well. No incubation was needed after the read buffer was added and before reading the plate.

Data analysis

The calculations used to establish calibration curves and determine concentration and data analysis were carried out using MSD Workbench 4.0 software. This software fits the standard curves using a four parameter logistic fit with $1/y^2$ weighting.

Brain/plasma amyloid-$\beta_{1\text{-}42}$ and amyloid-$\beta_{1\text{-}40}$ levels by ELISA

Fresh-frozen brain tissues were thoroughly homogenized in PBS buffer with 0.5% Triton™ X-100 (Sigma) and 1% protease inhibitor cocktail set I (Calbiochem) and then processed as previously described (Koronyo *et al.*, 2015). Blood was

immediately centrifuged after collection (730*g* for 10 min at 4°C) for plasma isolation. After determination of protein concentration with the aid of the Pierce BCA Protein Assay Kit (Thermo Scientific), concentrations of amyloid-β_{42} (Invitrogen KHB441) in the soluble and insoluble brain protein fractions and amyloid-β_{40} (Invitrogen KHB3481) in the plasma were analysed using a sandwich ELISA kit (Invitrogen) as per the manufacturer's instructions.

Cell viability assay

Amyloid-β_{42} films were dissolved in 60 mM NaOH, sonicated for 1 min in an ultra-bath sonicator, and diluted into cell culture media to the desired concentration. Aliquots of 10 µl were added to individual wells of 96-well microplates. Each well contained ~30 000 cells in a volume of 90 µl. After an incubation lasting ~15 h, 15 µl of MTT reagent was added to each well and the cells were incubated for 3 h at 37°C. SDS DMF HCl acetic acid stop solution (100 µl) was added to each well, and the plates were incubated overnight in the dark to ensure complete solubilization. The plates were then read using a microplate reader, and the absorbance at 570 nm (formazan product) minus the absorbance at 630 nm (background) was recorded. Controls included cells treated with NaOH only and 1 µM staurosporine (to induce apoptosis and yield maximal cell death). A minimum of six replicates were done for each treatment group, and the data from three independent experiments were combined and reported as mean ± standard error of the mean (SEM). The biological activity of amyloid-β was compared using the one-way analysis of variance Tukey test.

Preparation of low molecular weight amyloid-β_{42}

Low molecular weight (LMW) 99% HPLC purified amyloid-β_{42} peptide was synthesized in the UCLA Biopolymer Laboratory (Bitan and Teplow, 2005) or purchased from AnaSpec. Aggregate-free amyloid-β_{42} (LMW amyloid-β) was prepared as follows: Microcon YM-30 filters (EMD Millipore) were washed with 200 µl distilled deionized water. Amyloid-β was dissolved in 10% (v/v) 60 mM NaOH and 90% (v/v) 10 mM phosphate buffer, pH 7.4, at a concentration of 1 mg/ml. The solution was sonicated for 1 min and then placed into the washed 30 kDa filter. Following centrifugation at 14 000*g* for 20 min, the filtrate, LMW amyloid-β, was collected, and its concentration determined by optical absorption spectroscopy using a molar extinction coefficient of 1280 $M^{-1}cm^{-1}$ at 276 nm. Purified peptides were stored as lyophilizates at –20°C.

Preparation of amyloid-β_{42} fibrils

For fibrillar amyloid-β_{42}, LMW amyloid-β_{42} was prepared as described above, and the peptide preparation was incubated at 100 µM with orbital shaking at 37°C until fibril formation occurred, ~2 weeks (Koronyo *et al.*, 2015). The presence of fibrils was confirmed by electron microscopy.

Preparation of PICUP oligomeric amyloid-β_{42}

LMW amyloid-β was stabilized to 'freeze' oligomers using photo-induced cross-linking of unmodified proteins (PICUP) (Bitan *et al.*, 2001, 2003; Bitan and Teplow, 2004; Bitan, 2006) to yield a distribution of 'oligomeric amyloid-β'. Briefly, 2 mM Tris(2,2′-bipyridyl)dichlororuthenium(II) hexahydrate [$Ru(Bpy)^3$] (Aldrich) and 40 mM ammonium persulphate (APS) (Sigma) were prepared in distilled deionized water. An 18-µl aliquot of 80 µM LMW amyloid-β was placed in a PCR tube, followed by 1 µl $Ru(Bpy)^3$ and 1 µl APS. The sample was irradiated (150 W incandescent lamp) for 1 s, and the reaction was quenched immediately with 1 M dithiothreitol. Cross-linking reagents were removed by dialysis using 3.5 kDa MWCO Slide-A-Lyzer cassettes (Pierce) against 10 mM sodium phosphate, pH 7.4. More than five changes of buffer were completed, and the protein purity and concentration were confirmed using optical absorption spectroscopy.

Preparation of prion rod-like amyloid-β_{42}

LMW amyloid-β_{42} was prepared as described above, and the peptide preparation was diluted to 100 µM, incubated at room temperature without agitation for 9 h, and flash frozen.

Transmission electron microscopy

Ten microlitres of sample were spotted onto 400-mesh carbon-coated Formvar grids (Electron Microscopy Sciences) and incubated for 2 min. Each grid was then negatively stained with a 1% (v/v) solution of uranyl acetate (Ted Pella), passed through a 0.2-µm filter, which was immediately wicked off. TEM analysis was carried out using a JEOL 1200 EX at 80 kV (Fradinger *et al.*, 2005).

Flow cytometry

Brain tissues

After perfusion, the mouse brains were minced and digested for 30 min with 1.5 mg/ml collagenase IV (Worthington Biochemical Corp.) and DNase I (Stem Cell Technologies) at 37°C. After centrifugation, homogenization and washing, the pellet was suspended in 70% Percoll® (GE Healthcare) and then layered under a 30%/50% Percoll® step gradient. After 30 min of centrifugation at 800*g* at 4°C (without break), mononuclear cells at the interface of the 70% and 50% layers were collected and washed. For surface marker staining, the cells were blocked and stained (Table 1). For intracellular staining, the cells were fixed (eBioscience; #00-8222-49), permeabilized (eBioscience: #00-8333-56), and then stained (Table 1). Cells were treated with brefeldin A to stain for secreted cytokines (eBioscience: #00-4506-51).

In vitro assessment of fibril amyloid-β_{42} phagocytosis

Primary bone marrow or peritoneal-derived $CD115^+$ macrophages (wild-type and ACE^{10}) were exposed to preformed 1 nM HiLyte™ Fluor 647 amyloid-β_{1-42} (Anaspec) fibrils. At

specific time points (0, 15 and 60 min), the cells were stained and analysed by flow cytometry.

Data and statistical analysis

Data were analysed using GraphPad Prism v. 7.01 (GraphPad) software. Normally distributed data resulting from the IHC, ELISA, and flow cytometry analyses are expressed as means ± SEMs. One-way or two-way ANOVA with Sidak's and Bonferroni's post-tests was used for multiple comparisons (three or more means). The threshold for statistical significance was set at 0.05. For most behavioural testing, a power of 80% was obtained with 8–10 animals per group. For stereology or other semi- or fully quantitative analysis (i.e. q-IHC, ELISA), 6–8 mice per group have sufficient power to detect significance. Two-group comparisons were analysed using a paired or unpaired Student *t*-test. The statistical association between two or more variables was determined using Pearson's correlation coefficient (*r*) test (GraphPad Prism) with corrections for multiple analyses. Pearson's *r* indicates direction and strength of the linear relationship between two variables. Results are shown as mean ± SEM. Degrees of significance between groups are represented as follows: $^{*}P < 0.05$, $^{**}P < 0.01$, $^{***}P < 0.001$, and $^{****}P < 0.0001$.

Data availability

The data that support the findings of this study are available from the corresponding author, upon reasonable request.

Results

Reduced pathology in AD^{+} mice after partial ACE^{10} bone marrow replacement linked to brain and retinal monocyte recruitment

In our initial experiment, we tested bone marrow transplantation in $APP_{SWE}/PS1_{\Delta E9}$ double-transgenic mice (AD^{+} mice). Two-month-old mice (n = 22) received a high dose of radiation while placed inside a head-shielding device. Immediately afterward, the animals received an intravenous injection of either AD^{+} bone marrow (GFP^{-}AD^{+}ACE^{WT}; n = 7, three females and four males), control bone marrow (GFP^{+}AD^{-}ACE^{WT}; n = 7, two females and five males), or ACE^{10} bone marrow (GFP^{+}AD^{-}ACE^{10}; n = 8, three females and five males) (Fig. 1A and Supplementary Fig. 1A–C). Blood analysis 8 weeks post-transplantation showed that our protocol resulted in mice with chimeric bone marrow consisting of ~30–40% of cells from donor origin. At 7 months, the two groups with GFP-labelled bone marrow were examined using non-invasive retinal fluorescence imaging (Supplementary Fig. 1D) to track infiltration of GFP monocytes to CNS tissue using a rodent retinal Micron-III microscope (Koronyo *et al.*, 2012, 2017). AD^{+} chimeric mice with BM^{WT} had inflammatory cells surrounding amyloid-β plaques, including peripheral bone marrow-derived GFP^{+}CD45^{hi} monocytes (Fig. 1B). Analyses demonstrated reductions in amyloid-β plaque area (6E10^{+}), soluble brain amyloid-β_{1-42} levels (ELISA), GFAP^{+} cells, and GFAP^{+} area in mice that had received ACE^{10} bone marrow compared to AD^{+} control mice (47%, 31%, 33% and 33% decreases, respectively) (Fig. 1C–F). Figure 1G and H demonstrate less cortical amyloid-β plaques stained with curcumin, a method previously described (Koronyo-Hamaoui *et al.*, 2009, 2011; Koronyo *et al.*, 2017), and lower cortical GFAP^{+} astrocytosis. Interestingly, these effects were localized in the brain as no significant differences in plasma levels of amyloid-β_{1-40} and amyloid-β_{1-42} (ELISA) or their ratios were observed between the experimental groups (Supplementary Fig. 1E). Further, no significant differences were noted between females and males.

To characterize the types of infiltrating inflammatory cells within AD^{+} mouse brains, flow cytometry was used to quantitate brain inflammatory populations as indicated in Fig. 1I–L and Supplementary Fig. 1F–I. Side scatter and forward scatter, along with biomarkers of haematopoietic myelomonocytic cells such as CD11b, CD45, Ly6C, and F4/80, were identified and quantified in the brain within the GFP-negative (endogenous cells) versus GFP-positive (bone marrow-derived donor cells) populations (Fig. 1I and J). Furthermore, analyses of the expression of the three cytokines TNFα, TGFβ, and IL10 within these inflammatory cells in the brain were included. These analyses showed the presence of both GFP^{+} donor monocytes in the brains of AD^{+} animals, with a nearly 3-fold increase in ACE^{10} compared to ACE^{WT} monocytes (CD11b^{+}CD45^{hi}Ly6C$^{int/hi}$; Fig. 1K; P = 0.0101), while the microglia populations (GFP^{-}CD11b^{+}CD45$^{int/low}$Ly6C^{low}) were unchanged (data not shown).

Given the importance of TNFα in the induction of pro-inflammatory macrophage polarization and the pathogenesis of Alzheimer's disease, we examined TNFα expression by both GFP^{-}CD11b^{+}CD45$^{low-int}$ microglia and brain-infiltrating GFP^{+}CD11b^{+}CD45^{hi}Ly6C^{int-hi}F4/80^{hi} macrophages (Fig. 1L and Supplementary Fig. 1F and G). With regards to microglia, there was no difference in TNFα in any of the groups of mice (Supplementary Fig. 1F). In contrast, there was a significant and substantial 62% decrease in TNFα expression in ACE^{10} macrophages in those AD^{+} animals that had received GFP^{+}ACE^{10} bone marrow rather than GFP^{+}ACE^{WT} bone marrow ($P < 0.05$; Fig. 1L). Further, our flow cytometry analysis into the chimeric AD^{+}ACE^{10} mouse brains allowed us to compare TNFα in cerebral macrophages from endogenous, non-GFP (wild-type for ACE expression) versus donor marrow, GFP^{+} (with overexpression of ACE) sources in individual mice (Supplementary Fig. 1G). We found that those macrophages overexpressing ACE produced 58% less cerebral TNFα ($P < 0.05$). No significant differences were detected in TGFβ and IL10 levels in cerebral macrophages of chimeric AD^{+} mice (Supplementary Fig. 1H and I).

To investigate cerebral ACE^{10} macrophage phenotype further, we assessed insulin-like growth factor 1 (IGF1),

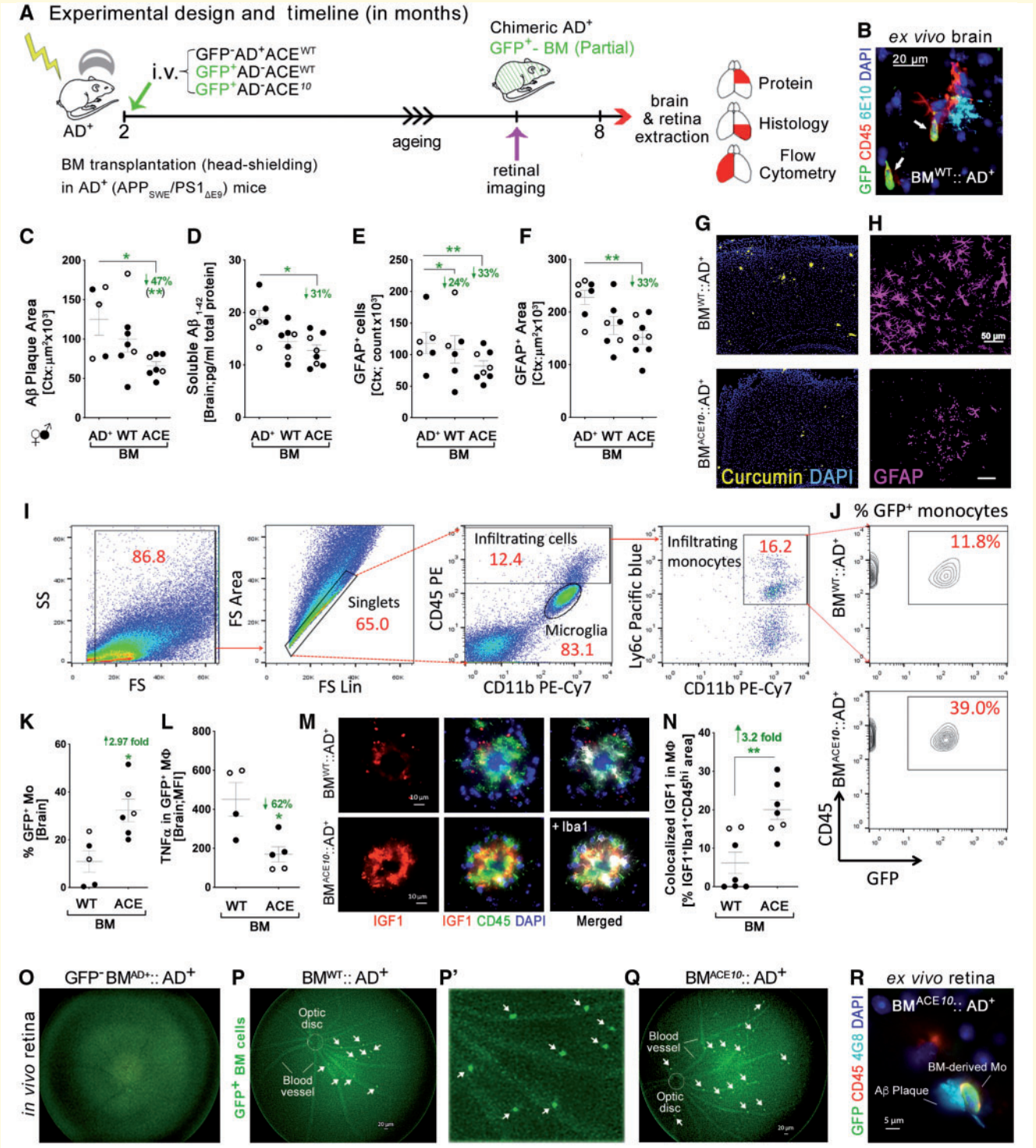

Figure 1 Beneficial effects of partial ACE^{10} bone marrow transplantation in APP$_{SWE}$/PS1$_{\Delta E9}$ transgenic mice. (**A**) Schematic illustration of experimental design and timeline. At 2 months of age, three groups of double-transgenic APP$_{SWE}$/PS1$_{\Delta E9}$ (AD$^+$) recipient mice (n = 22) underwent an irradiation procedure, with their heads shielded by a 3-inch-thick lead block. Mice then received a lethal dose of 950 rad irradiation for 11 min (Supplementary Fig. 1A–C). Immediately after irradiation, AD$^+$ recipient mice received an intravenous (i.v.) injection of 5 million bone marrow cells from one of three types of donor mice: GFP$^-$AD$^+$ACE^{WT}, GFP$^+$AD$^-$ACE^{WT}, or GFP$^+$AD$^-$ACE^{10}. The resulting BM^{WT}::AD$^+$, BM^{ACE10}::AD$^+$, and BM^{AD+}::AD$^+$ chimeric mice (n = 7–8 per group) had a partial (~30–40%) bone marrow transplantation. The two groups of GFP-labelled bone marrow chimeric AD$^+$ mice underwent retinal imaging at 7 months of age. Tissues were harvested for analysis from all three experimental groups when the animals were 8 months of age; the left hemisphere was used for flow cytometry, the right hindbrain for histology, and the right forebrain for protein analysis. (**B**) Representative fluorescence micrograph of the BM^{WT}::AD$^+$ chimeric mouse brain showing infiltrating monocytes (GFP$^+$/CD45^{hi}; arrows) near a 6E10$^+$ amyloid-β plaque site. Scale bar = 20 μm. (**C**) Quantitative IHC analysis of 6E10$^+$ amyloid-β plaque areas in brain cortices (Ctx) of BM^{WT}::AD$^+$, BM^{ACE10}::AD$^+$, and BM^{AD+}::AD$^+$ chimeric mice (n = 5–7 mice/group).

(continued)

associated with anti-inflammatory and neuro-regenerative functions (Gasparini and Xu, 2003; Butovsky *et al.*, 2006; Koronyo-Hamaoui *et al.*, 2009; Han *et al.*, 2016; Bianchi *et al.*, 2017; Spadaro *et al.*, 2017; Vannella and Wynn, 2017) in the brains of chimeric AD^+ACE^{10} mice compared to control mice (Fig. 1M and N and Supplementary Fig. 1J–O). Our immunohistochemistry data demonstrate a consistent 2.3-fold increase in cerebral IGF1 expression, and further, a substantial 2.5-fold increase surrounding Thio-S^+ amyloid-β plaques in chimeric AD^+ACE^{10} mice (Supplementary Fig. 1K and L; $P < 0.05$ and 0.0001). Moreover, cerebral IGF1 was predominantly expressed by $Iba1^+CD45^{high}$ brain-infiltrating monocytes and macrophages, with a significant 3.2-fold elevation of IGF1 expression in brain macrophages in chimeric AD^+ACE^{10} mice (Fig. 1M and N and Supplementary Fig. 1M and N; $P < 0.01$). A tight correlation was observed between cerebral IGF1 immunoreactive area and co-localized IGF1 within macrophages (Supplementary Fig. 1O; Pearson's $r = 0.92$, $P < 0.0001$), suggesting that infiltrating monocyte/macrophages are the main source of IGF1 in these chimeric AD^+ mice. Thus, there appears to be a fundamental difference between wild-type and ACE^{10} macrophages in their responses to an identical inflammatory environment induced by Alzheimer's disease in the brain.

Figure 1O–Q shows non-invasive retinal images from live AD^+ mice that had received bone marrow transplantation with either non-GFP AD^+ACE^{WT} (Fig. 1O), GFP^+-AD^-ACE^{WT} (Fig. 1P and P'), or GFP^+-AD^-ACE^{10} (Fig. 1Q). Numerous macrophages within the retina were observed (Fig. 1P and Q). Supplementary Videos 1 and 2 demonstrate the ability to track individual GFP^+ immune cells derived from wild-type and ACE^{10} bone marrow, respectively, in the live retina of an Alzheimer's disease model mouse. Further, detailed histological examination of *ex vivo* retinal immunohistochemistry imaging documents homing of ACE^{10} macrophages to amyloid-β plaque (Fig. 1R). This was seen far more consistently in those animals that had received bone marrow from ACE^{10} donors than in animals that had received bone marrow from an ACE^{WT} origin (Fig. 1P and Q).

Synaptic and cognitive preservation following peripheral blood enrichment of $CD115^+$ ACE^{10} monocytes

Another more translational strategy that we used to assess the relative contribution and potential therapeutic effect of ACE^{10} monocytes involved peripheral blood enrichment with $CD115^+$ monocytes. CD115 is the product of the *Csf1r* gene; monocytes that express this marker are often termed inflammatory monocytes and are recruited to inflamed sites to mediate tissue repair (Valero *et al.*, 2017). Previous work from our laboratory has established that adoptively transferred $CD115^+$ wild-type monocytes in AD^+ mice directly ameliorate amyloid-β neuropathology and lead to reduced neuroinflammation and preservation of cognitive function (Koronyo *et al.*, 2015). Our current findings demonstrate that ACE^{10} bone marrow can further reduce the neuropathology in AD^+ mice more than ACE^{WT} bone marrow; hence, the next step

Figure 1 Continued

(**D**) Sandwich ELISA analysis of cerebral soluble amyloid-β_{42} levels in AD^+ chimeric mice (n = 6–8 mice/group). (**E**) Quantitative IHC analysis of the cortical $GFAP^+$ reactive astrocyte cell count in AD^+ chimeric mice (n = 6–8 mice/group). (**F**) Quantitative IHC analysis of the cortical $GFAP^+$ reactive astrocyte area in AD^+ chimeric mice (n = 7 mice/group). (**G**) Representative micrographs of cortical amyloid-β plaques stained with curcumin in BM^{WT}::AD^+ versus BM^{ACE10}::AD^+ chimeric mice. (**H**) Representative micrographs of cortical $GFAP^+$ astrocytes in the same experimental groups. Scale bar = 50 μm (for **G** and **H**). (**I**) Flow cytometry analysis for cerebral infiltrating GFP^+ monocytes in AD^+ chimeric mice. Combinations of markers were used to identify microglia ($CD11b^+CD45^{int-low}GFP$) versus infiltrating monocyte subsets ($CD11b^+CD45^{hi}Ly6C^{hi}GFP^+$). (**J**) Representative flow cytometry map analysis showing increased infiltration of $CD11b^{hi}CD45^{hi}Ly6C^{hi}GFP^+$ ACE^{10} versus wild-type monocytes in AD^+ chimeric mice. (**K** and **L**) Quantitative flow cytometry analyses of cerebral inflammatory biomarkers in chimeric AD^+ mice following partial bone marrow transplantation. (**K**) Percentage of $GFP^+CD11b^{hi}CD45^{hi}Ly6C^{hi}F4/80^{low}$ monocytes (n = 5–6 mice/group), (**L**) TNFα expression in infiltrating $GFP^+CD11b^+CD45^{hi}Ly6C^{int-hi}F4/80^{hi}$ Mϕ (n = 4–5 mice/group). (**M**) Fluorescent micrographs of cortical brain regions stained against IGF1 (red) combined with Iba1 (white) CD45 (green) and nuclei (blue) in BM^{WT}::AD^+ versus BM^{ACE10}::AD^+ chimeric mice. Scale bars = 10 μm. Brain-infiltrating $Iba1^+CD45^{hi}$ Mo/Mϕ abundantly expressed IGF1 in BM^{ACE10}::AD^+ chimeric mice (*bottom*). (**N**) Quantitative IHC of % $IGF1^+$ area co-localized with Mo/Mϕ in BM^{WT}::AD^+ versus BM^{ACE10}::AD^+ chimeric mice (n = 7 mice/group). (**O**–**Q**) Representative non-invasive retinal fluorescence imaging of infiltrating GFP^+ bone marrow cells in living AD^+ chimeric mice. (**O**) A control AD^+ mouse that underwent bone marrow transplantation of GFP^-BM^{AD+} (GFP^-BM^{AD+}::AD^+). (**P**) Retinal fluorescent images from a GFP^+BM^{WT}::AD^+ mouse (**P'**, enlarged image). (**Q**) Retinal fluorescent images from a GFP^+BM^{ACE10}::AD^+ mouse (arrows indicate GFP^+ bone marrow cells). (**R**) Representative microscopic image obtained during the histological examination of a retina extracted from a BM^{ACE10}::AD^+ mouse whose retina had been previously imaged *in vivo*; *ex vivo* staining with GFP (green), CD45 (red), 4G8 (cyan), and DAPI (blue), validating the homing of GFP^+ACE^{10} monocytes to retinal amyloid-β plaques. Scale bar = 5 μm. Data from an individual mouse (filled circles for males and clear circles for females) as well as group mean ± SEM are shown. Fold increase and percentage decreases compared to control groups are shown in green. $^*P < 0.05$, $^{**}P < 0.01$. ns = non-significant, using one-way ANOVA and Bonferroni's post-test for three group comparisons. For two-group comparisons, paired or unpaired two-tailed Student *t*-tests were used. Aβ = amyloid-β; FS = forward scatter; SS = side scatter.

was to test the effects of blood enrichment with CD115$^+$ ACE^{10} monocytes (Fig. 2). The experimental procedure and timeline for adoptive transfer studies can be found in Fig. 2A–D (n = 23 AD$^+$ experimental mice and n = 7 non-transgenic naïve wild-type littermates; all males). Controls for this experiment were recipient AD$^+$ mice that had received monthly intravenous injections of PBS (vehicle). At 11 months, open field and Barnes maze behavioural tests were performed (Fig. 2E–K and Supplementary Fig. 2A) as previously described (Bernstein *et al.*, 2014*b*; Koronyo *et al.*, 2015). There were no differences in locomotor activity, neither rearing nor ambulatory movements, between any of the groups (Fig. 2E and F). Substantial differences in performance in the Barnes cognitive test, both in incorrect entries and latency times, were recorded during the training phase of the study and during the long-term memory retention and reversal phases (Fig. 2G–K and Supplementary Fig. 2A–C). Adoptive transfer of CD115$^+$ cells enhanced overall cognitive functions, with ACE^{10} monocytes consistently showing a trend of extended improvement.

In the training phase, AD$^+$ mice that had received CD115$^+$ monocytes with either ACE^{WT} or ACE^{10} showed a pattern of maze learning that was essentially identical to that of wild-type mice (Fig. 2G and Supplementary Fig. 2A). In contrast, AD$^+$ mice that had received PBS displayed impaired training compared to wild-type mice. In the long-term memory retention test (Day 7), during the reversal phase (Day 8), and in the spatial memory analysis at Day 9, we observed significant differences between mice receiving CD115$^+$ ACE^{10} cells and those receiving PBS controls. Mo^{ACE10}-treated mice displayed a pattern of learning equivalent to that of wild-type mice, which was also superior to recipients of the Mo^{WT} cells (Fig. 2H–K and Supplementary Fig. 2B and C).

Immunohistochemical analysis of 6E10$^+$ plaque area in the hippocampus, cingulate cortex, and total brain shows that AD$^+$ mice that had received an infusion of CD115$^+$ (predominantly ACE^{10}) monocytes had fewer hippocampal and total brain plaques than AD$^+$ mice that had received only PBS vehicle ($P < 0.05$, Fig. 2L and Supplementary Fig. 2D–F). Analysis of vascular Thio-S$^+$ amyloid-β burden calculated as CAA score (Rentsendorj *et al.*, 2018) revealed significant 56% and 82% reductions in CAA scores in AD$^+$ mice recipients of both BM^{WT} and BM^{ACE10}, respectively, compared to the control group (Fig. 2M and Supplementary Fig. 2I–M; $P < 0.0001$). A significant reduction in CAA scores was further noted in recipients of BM^{ACE10} versus BM^{WT} in hippocampal and cortical regions (Fig. 2M and Supplementary Fig. 2L and M; $P < 0.05$). Analysis of synaptic biomarkers indicated a significant preservation of both pre- (VGluT1) and post- (PSD-95) synapses by blood enrichment with CD115$^+$ ACE^{10} monocytes, promoting synaptic protection (Fig. 2N and Supplementary Fig. 2G and H; $P < 0.05$–$P < 0.001$).

Enhanced binding and uptake of pathological amyloid-β$_{42}$ conformers and surface expression of scavenger receptors in ACE^{10} macrophages

Next, we characterized ACE-overexpressing macrophages for their ability to recognize, bind, internalize, and process defined structures of amyloid-β associated with Alzheimer's disease neuropathology. To this end, we performed an experiment in which bone marrow cells were harvested from wild-type and ACE^{10} mice and then cultured for 6 days with MCSF to generate mature macrophages (Fig. 3A). On Day 7, these cells were mixed with well-defined and characterized populations of amyloid-β$_{1-42}$ fibrils, amyloid-β$_{1-42}$ prion rod-like structures, or cross-linked-stabilized soluble amyloid-β$_{1-42}$ oligomers (Fig. 3A and B). The identity of amyloid-β products was confirmed by SDS-PAGE and TEM (Fig. 3B and C). Another control group for this experiment included untreated cells, which were not exposed to amyloid-β. Figure 3D shows surface binding of fibril amyloid-β$_{42}$ to a class A type 1 scavenger receptor, Scara1, on the cell membrane of ACE^{10} macrophages (0 min time point); macrophages were immunostained for anti-amyloid-β (6E10), Scara1 (CD204), and nuclei (DAPI; Fig. 3D).

Quantitative ICC analysis indicates substantial 4.9-fold and 2-fold increases of surface fibril amyloid-β$_{42}$ and oligomer amyloid-β$_{42}$ binding, respectively, in ACE^{10} macrophages as compared with wild-type macrophages (Fig. 3E; P = 0.001 and P = 0.02, respectively). Membrane scavenger receptors such as Scara1, class B scavenger receptor CD36, triggering receptor expressed on myeloid cells 2 (TREM2), and CD163 have been implicated in macrophage activation and increased phagocytosis of amyloid-β in Alzheimer's disease (Hickman *et al.*, 2008; Yamanaka *et al.*, 2012; Frenkel *et al.*, 2013; Pey *et al.*, 2014; Kim *et al.*, 2017). We observed significant increases in baseline Scara1, TREM2, CD163, and CD36 surface expression in untreated ACE^{10} versus wild-type macrophages (Fig. 3F, Supplementary Fig. 3A and B and Supplementary Table 1; $P < 0.01$–0.0001). These receptors have been associated with Alzheimer's disease and specifically facilitate amyloid-β uptake by microglia and/or macrophages but have never been studied in ACE^{10} macrophages or in response to defined and stabilized populations of amyloid-β$_{42}$ oligomers. We also found that surface expression of TREM2 and Scara1 was increased in ACE^{10} macrophages at the 0-min time point and 5 min after exposure to fibril amyloid-β$_{42}$ (Fig. 3F–H and Supplementary Fig. 3C; $P < 0.05$–0.0001) but not in response to amyloid-β$_{42}$ prion rod-like structures or soluble oligomers (Fig. 3F and G). As early as 5 min after contact and phagocytosis of fibril amyloid-β$_{42}$, intracellular amyloid-β$_{42}$ staining was visible in the cell processes and soma of wild-type macrophages, and more prominently in ACE^{10} macrophages (Fig. 3H). Interestingly, baseline MHC-II expression was lower by 49% in the

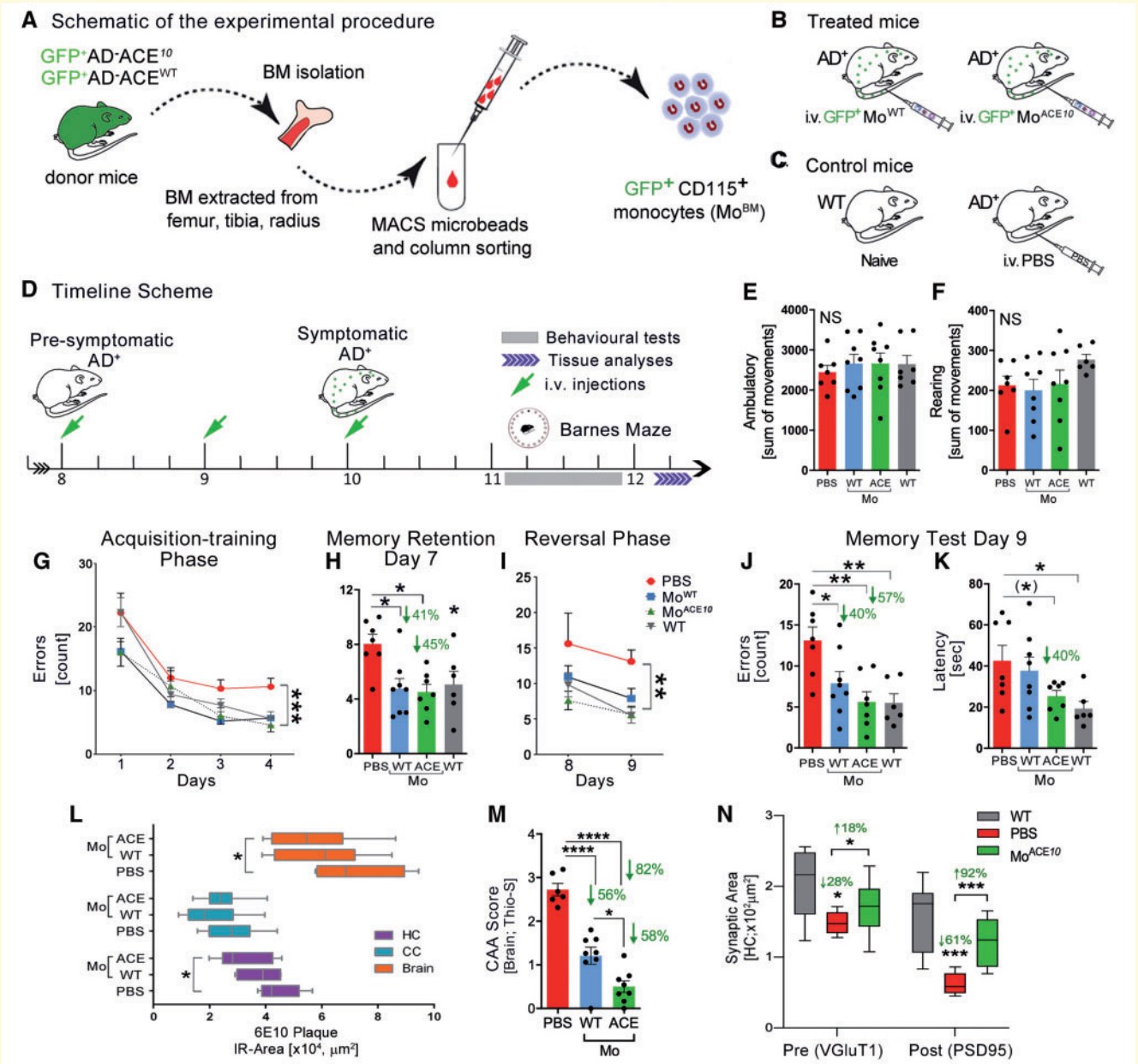

Figure 2 Cognitive preservation and restricted pathology following adoptive transfer of a CD115$^+$ ACE^{10} monocyte subset in AD$^+$ mice transgenic mice. (**A**–**C**) Schematic representation of experimental procedure and treatment groups. (**A**) CD115$^+$ monocytes (Mo^{BM}) were isolated from the bone marrow of GFP$^+$ donor mice and enriched by MACS microbeads and an anti-CD115 antibody column sorting procedure. (**B**) Mo^{BM} were then intravenously (i.v.) injected into the tail vein of AD$^+$ recipient mice (n = 8 mice/group, all males). (**C**) Additional control groups included naïve wild-type (WT) mice and AD$^+$ mice injected with PBS (n = 7 mice/group, all males). (**D**) Schematic timeline of the *in vivo* preclinical experiment. Pre-symptomatic AD$^+$ mice exhibiting neuropathology at 8 months of age received monthly injections of 5–6 million GFP$^+$Mo^{WT} or GFP$^+$Mo^{ACE10} or PBS for 3 months (immunization regimen indicated by green arrows). At 11 months, mice underwent behavioural tests followed by tissue collection and analysis when 12 months of age. (**E** and **F**) Open field test in all AD$^+$ treatment and naïve wild-type groups measuring: (**E**) ambulatory and (**F**) rearing activity. (**G**–**K**) Cognitive functions assessed by the Barnes maze test in both monocyte-treated groups as compared to the control PBS-injected group and naïve cognitively normal wild-type group (n = 6–8 mice/group). Incorrect entries (errors) for the following: (**G**) acquisition-training phase (Days 1–4), (**H**) memory retention (Day 7), (**I**) reversal phase (Days 8 or 9), and (**J** and **K**) memory test at Day 9. (**J**) Errors and (**K**) escape latency (s). (**L**) Quantitative IHC analysis of 6E10$^+$ amyloid-β plaque areas in the hippocampus (HC), cingulate cortex (CC), and total brain in Mo^{WT}- and Mo^{ACE10}-treated versus PBS-injected AD$^+$ mice (n = 7–8 mice/group). (**M**) CAA score assessed as vascular Thio-S$^+$ in AD$^+$ mice (n = 6–8 mice/group). Data from an individual mouse as well as group mean ± SEM are shown. (**N**) Quantitative IHC analysis of hippocampal pre-(VGluT1$^+$) and postsynaptic (PSD95$^+$) areas in Mo^{ACE10}-treated mice compared to PBS-injected control AD$^+$ and naïve wild-type mice (n = 6–8 mice/group). Data from individual mice, lower and upper quartiles (as lower and upper horizontal lines in box), median (midline within box), and minimum/maximum values (whiskers), are shown. Percentage increase and decrease compared to control groups are shown in green. $^*P < 0.05$, $^{**}P < 0.01$, $^{***}P < 0.001$, $^{****}P < 0.0001$. ns = non-significant, by two-way or one-way ANOVA and Bonferroni's post-test. Significance between two-groups by unpaired two-tailed Student t-test. IR = immunoreactive.

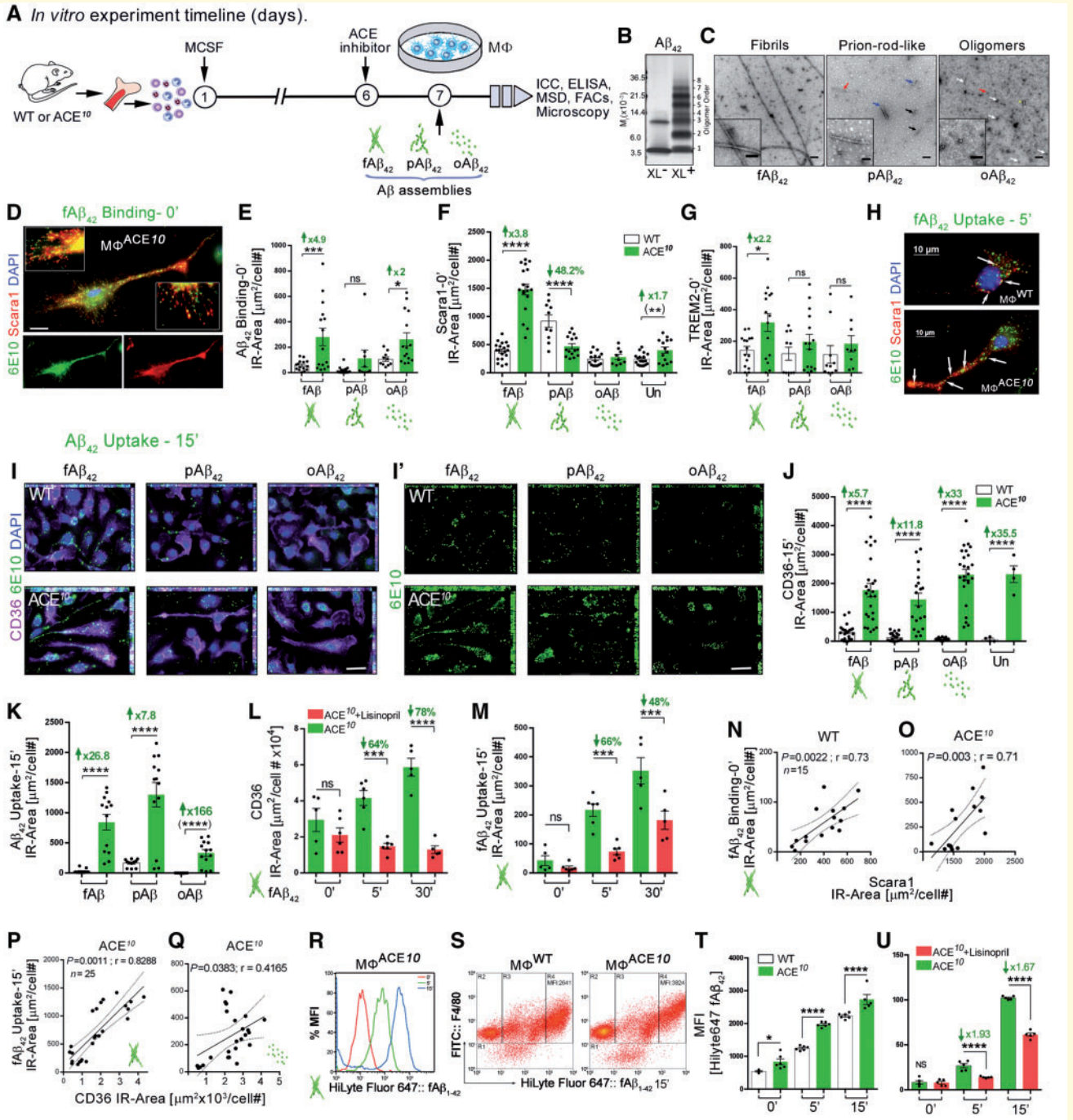

Figure 3 Enhanced surface recognition and uptake of diverse amyloid-β$_{42}$ conformers by ACE^{10} macrophages. (**A**) Design and timeline of *in vitro*. Bone marrow was isolated from young wild-type (WT) and ACE^{10} mice (8–12 weeks old) and cultured for 6 days in MCSF-enriched media, generating primary macrophage cultures (Mϕ^{WT} and Mϕ^{ACE10}, respectively). On Day 7, Mϕ were either unstimulated (Un) or stimulated by one of the three amyloid-β forms: fibrils (fAβ$_{42}$), prion rod-like structures (pAβ$_{42}$), or cross-linked oligomers (oAβ$_{42}$). Mϕ^{ACE10} were analysed and compared to control Mϕ^{WT} for cell surface amyloid-β$_{42}$ binding (pre-chilled on ice; binding – 0 min) and receptor expression as well as uptake of amyloid-β$_{42}$ species at incremental time points from 5 min up to 60 min (incubated at 37°C; uptake: 5, 15, 30 min). Cells and media were isolated and further analysed using various methods including ICC, flow cytometry (FC), and quantitative protein analysis. (**B**) Forms of non-cross-linked (non-XL) and cross-linked (oAβ) amyloid-β$_{42}$. Oligomers as large as an octamer are observed. (**C**) Negative stain TEM micrographs of amyloid-β$_{42}$ assemblies. *Left*: Fibrillar amyloid-β (fAβ$_{42}$) displayed long fibrils of ~10 nm diameter with a twisted morphology typically comprising two smaller filaments. *Middle*: Prion rod-like amyloid-β$_{42}$ (pAβ$_{42}$) displayed short (<300 nm) straight rods comprising multiple filaments (blue arrows). Narrower (~5 nm) rod-like structures appeared to comprise twisted double filaments (black arrows). The assembly indicated by the red arrow is shown in the *inset* at higher magnification. *Right:* Cross-linked oligomers (oAβ$_{42}$) displayed mainly quasi-spherical assemblies (white arrows) with diameters of 5–8 nm. The assembly indicated by the red arrow is shown in the *inset* at higher magnification. A rare rod-like structure (yellow asterisk) was also observed. Scale bars = 100 nm or 50 nm (*insets*). (**D**) Representative

(continued)

ACE^{10} macrophages (Supplementary Table 1; $P < 0.01$). A summary of key *in vitro* findings comparing ACE^{10} and wild-type macrophages can be found in Supplementary Table 1.

To assess the macrophages' ability to uptake amyloid-β_{42} species at later time points (15, 30, and 60 min), we conducted a series of experiments presented in Fig. 3I–U, Supplementary Table 1, and Supplementary Fig. 3. Figure 3I displays the major differences detected in macrophage uptake of different amyloid-β_{42} conformers after 15 min of exposure, with fibrils being the most efficiently phagocytosed and soluble oligomers the least engulfed by these cells (Supplementary Fig. 3D–F). Quantitative ICC analysis shows that surface CD36 expression by ACE^{10} macrophages was substantially and consistently increased as compared to wild-type macrophages (Fig. 3J; $P < 0.0001$), along with increased intracellular amyloid-β_{42} uptake 15 min after exposure to all three forms of amyloid-β (Fig. 3K; $P < 0.05$–0.0001). Moreover, the expression of CD36 as well as the uptake of fibril amyloid-β_{42} at 5 and 30 min were found to be dependent on ACE catalytic activity, since overnight treatment with the ACE inhibitor lisinopril significantly decreased both (Fig. 3L and M). Interestingly, in ACE^{10} macrophages treated with lisinopril, CD36 expression was decreased and fibril amyloid-β_{42} uptake increased over time during a 30-min culture period, while remaining substantially lower compared to their values in the enzymatically uninhibited ACE^{10} macrophages (Fig. 3L and M). Supplementary Table 1 summarizes the main findings on amyloid-β surface binding and uptake as well as the expression of scavenger receptors, the immune profile, and the morphology of wild-type versus ACE^{10} macrophages.

Analysis of discrete wild-type and ACE^{10} macrophage populations to determine potential associations between amyloid-β_{42} binding/uptake and surface expression of the scavenger receptors Scara1 and CD36, using Pearson's r correlations, revealed strong and direct relationships in both cell genotypes (Fig. 3N and O; $r = 0.73$, $P = 0.0022$ for wild-type; $r = 0.71$, $P = 0.003$ for ACE^{10}, for Scara1). Further, there were direct correlations between amyloid-β_{42} fibril and amyloid-β_{42} oligomer uptake after a 15-min incubation and the expression level of CD36 in ACE^{10} macrophages (Fig. 3P and Q; $r = 0.83$ and $P = 0.001$ for fibril amyloid-β_{42}; $r = 0.42$, $P = 0.038$ for oligomer amyloid-β_{42}). The strong correlation between CD36 expression and amyloid-β uptake was also true for prion rod-like amyloid-β_{42} uptake after 15 min in both wild-type and ACE^{10} macrophages (Supplementary Fig. 3K and L; $r = 0.83$ and 0.76, respectively, and $P < 0.0001$). Extended correlations are shown in Supplementary Fig. 3G–L.

Using quantitative flow cytometry analysis, we validated increased binding and uptake of fluorescently labelled HiLyte 647-fibril amyloid-β_{42} in ACE^{10} versus wild-type macrophages, from both bone marrow and peritoneal sources, as well as reversal effects following inhibition of ACE catalytic domains (Fig. 3R–U and Supplementary Fig. 3M–P). Flow cytometry-based quantitative analyses confirmed the aforementioned ICC analysis and demonstrated that the rate of amyloid-β_{42} fibril phagocytosis by

Figure 3 Continued

fluorescence micrograph of $M\phi^{ACE10}$ prestimulated with fibril amyloid-β_{42} on ice (at the 0-min time point) and immunolabelled for Scara1 (red), human amyloid-β (6E10; green), and nuclei (blue). Abundance of co-surface labelling of $Scara1^+$ and fibril amyloid-β_{42} (yellow spots) on the $M\phi^{ACE10}$ cell body and processes was detected, indicating large amounts of fibril amyloid-β_{42} bound to surface Scara1. (**E**) Quantitative ICC analysis of a $6E10^+$ immunoreactive (IR) area for cell surface binding of the three amyloid-β_{42} species (250 nM each) at the 0-min time point in $M\phi^{ACE10}$ versus $M\phi^{WT}$. (**F**) Quantitative ICC analysis of surface Scara1 expression in ACE^{10} versus wild-type Mϕ that were either untreated or in the presence of different amyloid-β_{42} forms at the 0-min time point. (**G**) Quantitative ICC analysis of TREM2 expression in ACE^{10} versus wild-type Mϕ following prestimulation by the different forms of amyloid-β_{42} (250 nM each). (**H**) Representative fluorescence micrograph of $M\phi^{WT}$ and $M\phi^{ACE10}$ cells that were incubated for 5 min with 250 nM fibril amyloid-β_{42} and later immunolabelled for Scara1 (red), human amyloid-β (6E10; green), and nuclei (blue). Amyloid-β_{42} fibrils are seen in intracellular vesicles within these phagocytic cells (white arrow). (**I**) Panel of representative fluorescence micrographs of $M\phi^{WT}$ and $M\phi^{ACE10}$ cells following a 15-min incubation with three different amyloid-β_{42} forms immunolabelled for scavenger receptor type B CD36 (purple), human amyloid-β (6E10; green), and nuclei (blue). (**I'**) Separated single channel (cy2) for intracellular amyloid-β_{42} uptake. (**J**) Quantitative ICC analysis of CD36 expression (μm^2/cell number) in ACE^{10} versus wild-type Mϕ that were either untreated or exposed to different amyloid-β_{42} forms (250 nM) for 15 min. (**K**) Quantitative ICC analysis of $6E10^+$ immune-reactive area (μm^2/cell number) for intracellular uptake of the three amyloid-β_{42} species (250 nM) for 15 min by $M\phi^{ACE10}$ versus $M\phi^{WT}$. (**L** and **M**) Quantitative ICC analysis of (**L**) CD36 expression and (**M**) amyloid-β uptake by untreated versus ACE-inhibitor pretreated (1 μM lisinopril overnight in RPMI media + 0.3% BSA) $M\phi^{ACE10}$, following exposure to 100 nM fibril amyloid-β_{42} for either 0, 5 or 30 min. (**N**–**Q**) Individual correlation analysis of the following: (**N** and **O**) surface fibril amyloid-β_{42} and Scara1 immunoreactive area at the binding time point in (**N**) $M\phi^{WT}$ and (**O**) $M\phi^{ACE10}$ (n =15 wells); (**P** and **Q**) surface fibril/oligomer amyloid-β_{42} and CD36 expression in $M\phi^{ACE10}$ following a 15-min exposure to either fibril amyloid-β_{42} or oligomer amyloid-β_{42}. (**R**) Representative peak analysis in percentage mean fluorescence intensity (MFI) of $M\phi^{ACE10}$ uptake of HiLyte Fluor 647-labelled fibril amyloid-β_{42} at the 0-, 5-and 15-min time points. (**S**) Representative flow cytometry images of HiLyte Fluor 647-labelled fibril amyloid-β_{42} MFI at the 15-min time point by $F4/80^+$-$M\phi^{WT}$ versus -$M\phi^{ACE10}$. (**T** and **U**) Quantitative flow cytometry analysis of HiLyte Fluor 647-labelled fibril amyloid-β_{42} MFI uptake at the 0-, 5- and 15-min time points by (**T**) $M\phi^{WT}$ or $M\phi^{ACE10}$ and by (**U**) untreated and lisinopril pretreated $M\phi^{ACE10}$. The group mean ± SEM as well as the fold reduction or increase and percentage decrease between groups are shown. $^*P < 0.05$, $^{**}P < 0.01$, $^{***}P < 0.001$, $^{****}P < 0.0001$; ns = non-significant, by two-way or one-way ANOVA and Bonferroni's or Sidak's post-test, while asterisks in parentheses signify a two-group comparison using the unpaired two-tailed Student t-test.

ACE^{10} macrophages is significantly faster than that by wild-type macrophages in the first 5, 15 and 60 min of uptake assays (Fig. 3T and Supplementary Fig. 3M–P). Interestingly, the ACE inhibitor lisinopril also had effects on wild-type macrophages (peritoneal), significantly reducing phagocytosis of amyloid-β_{42} fibrils by >50% (Supplementary Fig. 3P), suggesting a role for endogenous ACE in macrophage-mediated fibril amyloid-β_{42} phagocytosis.

Superior endosomal-lysosomal and extracellular degradation of amyloid-β_{42} conformers by ACE^{10} macrophages

We next studied the capacity of ACE^{10} macrophages for intra- and extracellular processing and degradation of the three types of amyloid-β and the intracellular localization of these amyloid-β_{42} species (Fig. 4). We conducted a series of studies using bone marrow-derived ACE^{10} and wild-type macrophages (Fig. 3A–C). Initial studies of wild-type macrophages showed that when cells were exposed to fibril amyloid-β_{42}, the autophagy marker Beclin-1 relocated to the cell nucleus (Fig. 4A). No difference in Beclin-1 expression was detected in ACE^{10} versus wild-type macrophages (data not shown). In contrast to Beclin-1 expression, fibril amyloid-β_{42} appears to co-localize within early endosomes (EEA1) and lysosomal associated membrane proteins 1 and 2 (Lamp-1 and Lamp-2) within lysosomal vacuoles (Fig. 4B). Further analysis of amyloid-β intake after a 15-min exposure to fibril amyloid-β_{42}, prion amyloid-β_{42}, and oligomer amyloid-β_{42} showed co-localization of the amyloid-β peptides within early endosomes (Fig. 4C–F). The uptake of amyloid-β_{42} conformers and co-localization in the EEA1$^+$ endosomes was more apparent in ACE^{10} macrophages than in wild-type cells. This was observed for both the fibrillar and the soluble oligomeric forms of amyloid-β_{42}, although it was more intense for the fibrillar form (Fig. 4C–F). A systematic evaluation of the uptake of fibril, prion, and oligomer amyloid-β_{42} species by ACE^{10} versus wild-type macrophages was undertaken. Evaluation of the amyloid-β immunoreactive area within EEA1$^+$ endosomes (Fig. 4G) revealed that ACE^{10} cells consistently had greater amounts of amyloid-β in the endosomal-lysosomal pathway, presumably fated for intracellular degradation. The larger increases in the ACE^{10} macrophages were most pronounced for the soluble amyloid-β oligomers, as compared to prion rod-like structures and fibrils, as they took up far more soluble amyloid than that observed in wild-type cells (Fig. 4G and H; 21- to 40-fold increases, $P < 0.001$–0.05).

To elucidate the relative abilities of wild-type and ACE^{10} macrophages to degrade amyloid-β *in vitro*, cells from each genotype were cultured with fibril amyloid-β_{42} and monitored for 18, 20 and 24 h (Fig. 4I and Supplementary Fig. 4). At the end of this period, ELISA was performed to measure extracellular amyloid-β_{42} levels in the supernatant. There was a substantial reduction (81%) in extracellular amyloid-β_{42} concentration in the media of ACE^{10} macrophages compared to wild-type cell media (Fig. 4I; $P < 0.001$). We further performed an experiment in which ACE^{10} macrophages were allowed to take up and degrade fibril amyloid-β_{42} over 30 min in the presence or absence of lisinopril (Fig. 4J). A subset of ACE^{10} macrophages was treated under the same conditions in an ice bath (0°C) as a control. Amyloid-β_{42} concentrations in the combined media and cell fraction of macrophages were analysed by performing ELISA. Again, these data suggest that clearance of fibril amyloid-β_{42} is dependent on ACE catalytic activity, as the group of ACE^{10} macrophages treated with lisinopril had significantly higher amyloid-β_{42} concentrations than cells in which ACE was catalytically active (Fig. 4J; $P < 0.0001$).

Pro-healing immune profile of ACE^{10} macrophages exposed to Alzheimer's disease-related amyloid-β forms

To understand the biology of macrophages in response to amyloid-β forms, both wild-type and ACE^{10} bone marrow-derived macrophages were subjected to amyloid-β_{42} fibrils and oligomers, and their morphologies and immune phenotypes were assessed (Fig. 5 and Supplementary Fig. 5). As seen in Fig. 5A and C, ACE^{10}, as opposed to wild-type macrophages, express ~30% less iNOS and 80% more arginase-1 prior to amyloid-β_{42} fibril exposure ($P < 0.05$–0.01; Supplementary Fig. 5A and B). These differences became less apparent for arginase-1 after 5 min exposure to amyloid-β_{42} peptides (Fig. 5C). The 30% reduction of iNOS expression in ACE^{10} macrophages, compared to wild-type macrophages, was sustained even after 1-h incubation with soluble amyloid-β_{42} oligomers (Supplementary Fig. 5A). Further, considerable increases in expression of the amyloid-β-degrading enzyme MMP9 were observed in ACE^{10} macrophages, both when unstimulated and after exposure to amyloid-β_{42} fibrils over time (Fig. 5D and E; 1.6–2.5-fold increase, $P < 0.001$–0.0001). Noticeably, there was a clear difference in the physical form of the cells (Fig. 5F). The ACE^{10} macrophages were significantly more elongated and the percentage of elongated cells was higher than that in wild-type cells in the unstimulated state (Fig. 5G; 2.2- and 4.4-fold increase, respectively, $P < 0.001$). Exposing these cells to fibril amyloid-β_{42} for either 5 or 30 min resulted in an increased ACE^{10}-macrophage aspect ratio (elongation factor), determined as the quotient of maximum cell process length over cell body width (Fig. 5H; 2.0- and 1.7-fold increase, respectively, $P < 0.0001$). Hence, the cell processes of wild-type macrophages were consistently shorter than the processes of ACE-enhanced macrophages over time (Fig. 5F–H). This type of elongated macrophage morphology was previously associated with an anti-

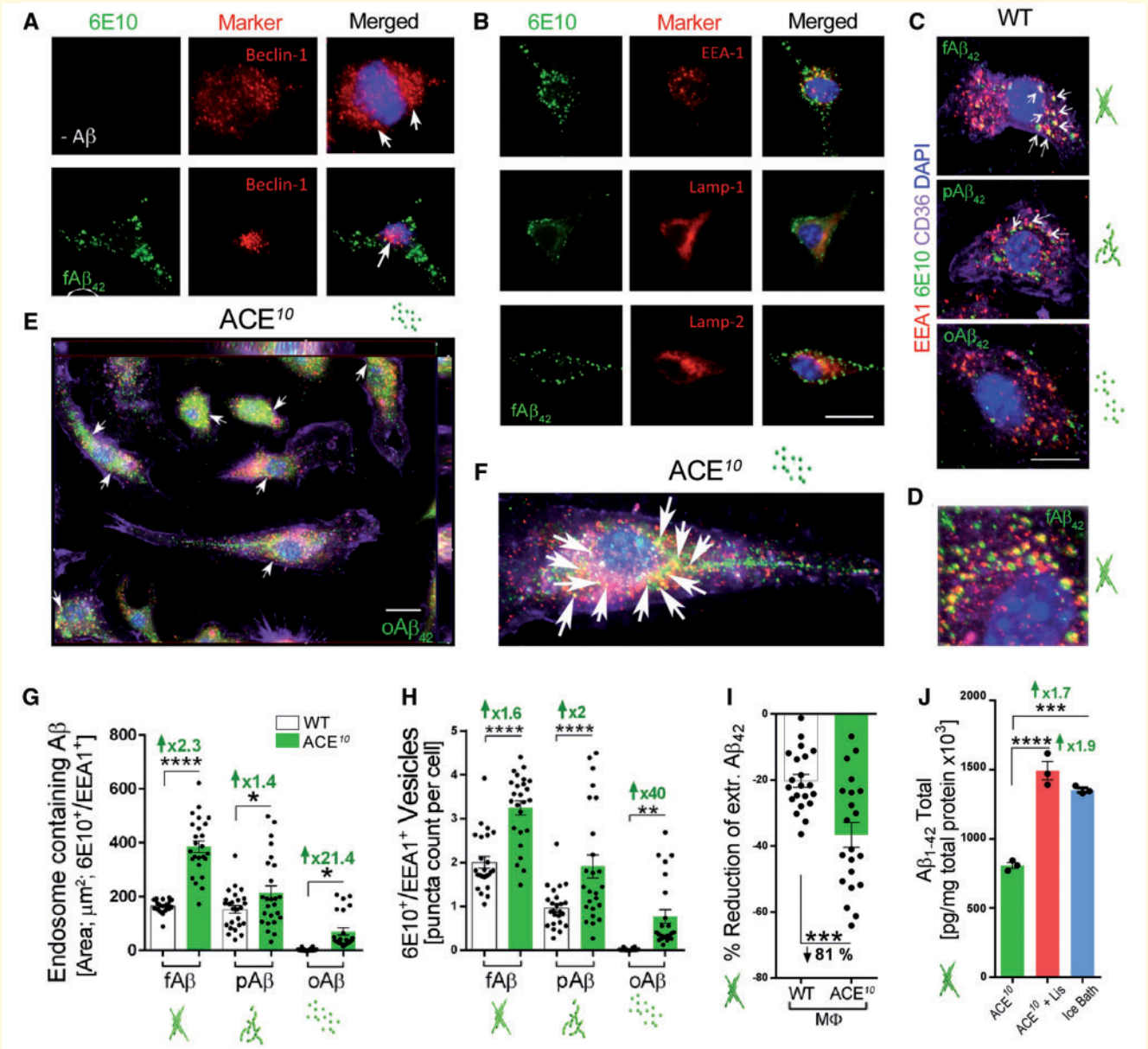

Figure 4 Intra- and extracellular degradation of pathological amyloid-β_{42} species by ACE^{10} macrophages. (**A**) Representative fluorescence micrograph of unstimulated (*top*) and fibril amyloid-β_{42} stimulated (*bottom*) Mϕ^{WT} immunolabelled for human amyloid-β (6E10; green), autophagy marker Beclin-1 (red), and nuclei (blue). Merged channel panels show that in response to fibril amyloid-β_{42}, Beclin-1 protein moves to the nuclei (white arrows). (**B**) Representative fluorescence micrograph panel of fibril amyloid-β_{42} (fAβ_{42}) stimulated Mϕ^{WT} immunolabelled for human amyloid-β (6E10; green), endosomal markers (EEA1, Lamp-1, Lamp-2, red), and nuclei (blue). (**C** and **D**) Representative fluorescence micrograph of Mϕ^{WT} stimulated with the different fibril , prion rod-like and oligomer amyloid-β_{42} forms for 15 min and immunolabelled for human amyloid-β (6E10; green), endosomal marker EEA1 (red), surface scavenger receptor CD36 (purple), and nuclei (blue). White arrows indicate co-localizing of intracellular amyloid-β_{42} within EEA1$^+$ vesicles. (**D**) Higher magnification image of co-localized fibril amyloid-β_{42} within EEA1$^+$ endosomes in Mϕ^{WT} (yellow spots). (**E** and **F**) Representative fluorescence micrograph of Mϕ^{ACE10} exposed to oligomer amyloid-β_{42} (100 nM for 15 min) and immunolabelled for human amyloid-β (6E10; green), endosomal marker EEA1 (red), surface scavenger receptor CD36 (purple) and nuclei (blue). White arrows indicate 6E10$^+$ and EEA1$^+$ co-localization. (**F**) Higher magnification image of co-localized oligomer amyloid-β_{42} within EEA1$^+$ endosomes in Mϕ^{ACE10} (white arrows). (**G** and **H**) Quantitative analysis of co-localized 6E10$^+$ and EEA1$^+$ immunoreactive area in unstimulated and fibril, prion rod-like and oligomer amyloid-β_{42}-stimulated Mϕ^{WT} or Mϕ^{ACE10}: (**G**) 6E10-IR area per macrophage and (**H**) count of 6E10$^+$/EEA1$^+$ vesicles using puncta count per macrophage. (**I**) Quantitative normalized analysis of percentage reduction of extracellular fibril amyloid-β_{42} in media of Mϕ^{WT} versus Mϕ^{ACE10} over 18, 20 and 24 h. (**J**) Quantitative ELISA analysis of total intra- and extracellular amyloid-β_{42} levels in the media and cell fraction of Mϕ^{ACE10}, following fibril amyloid-β_{42} for 30 min and either untreated, lisinopril pretreated (1 μM lisinopril overnight in RPMI media + 0.3% BSA), or pre-placed in ice bath. The group mean ± SEM as well as fold increase and percentage decrease between groups are shown. $^*P < 0.05$, $^{**}P < 0.01$, $^{***}P < 0.001$, $^{****}P < 0.0001$. ns = non-significant, by two-way or one-way ANOVA and Bonferroni's post-test.

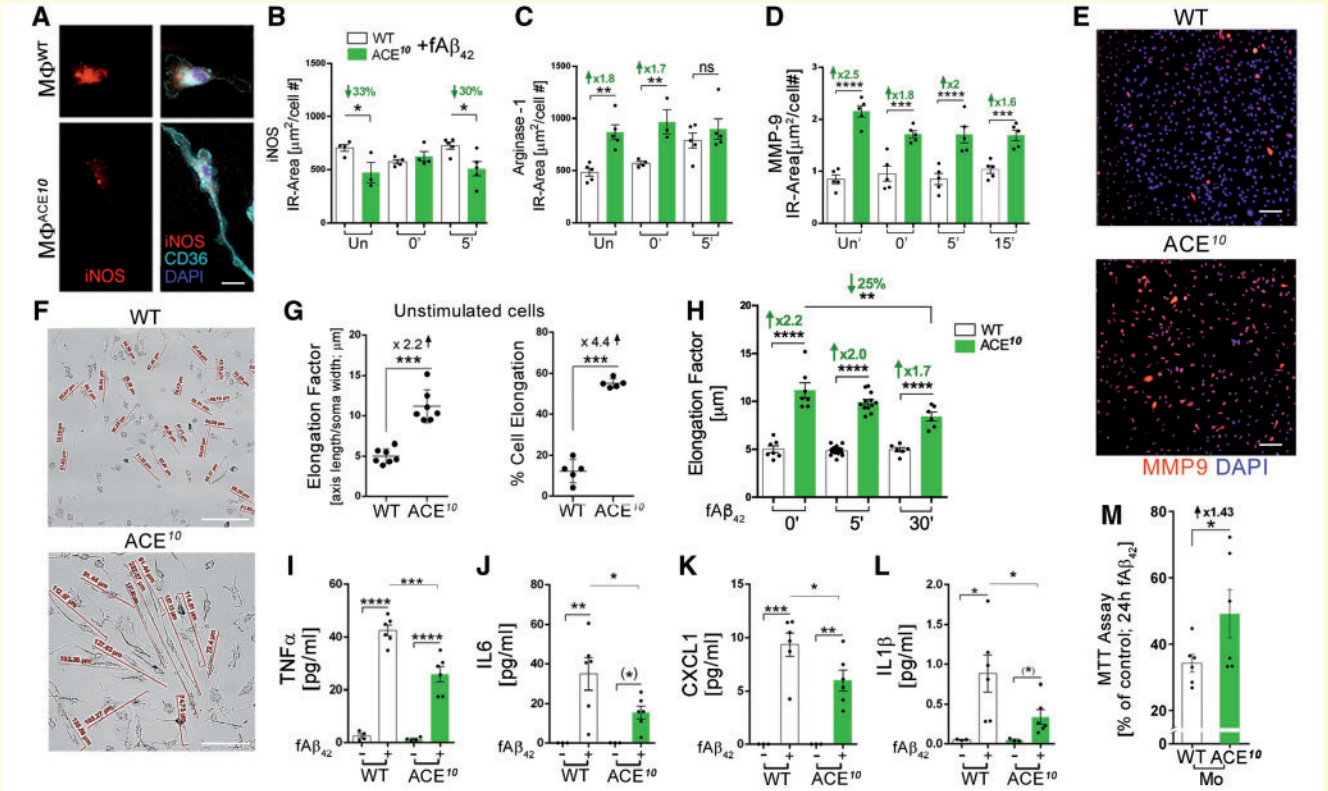

Figure 5 ACE overexpression in macrophages promotes a pro-healing, alternatively activated immune profile. (**A**) Fluorescence micrographs of inducible nitric oxide synthase (iNOS, red), scavenger receptor CD36 expression (cyan), and nuclei (blue) in $M\phi^{ACE10}$ versus $M\phi^{WT}$ (merged image on *right*). (**B**–**D**) Quantitative analysis showing (**B**) iNOS, (**C**) arginase-1, and (**D**) MMP9 in the immunoreactive area of unstimulated (Un) and fibril amyloid-β_{42}-stimulated $M\phi^{ACE10}$ and $M\phi^{WT}$ at the 0- and 5-min time points. (**E**) Representative fluorescence micrographs of $M\phi^{WT}$ and $M\phi^{ACE10}$ immunolabelled for MMP-9 (red) and nuclei (blue). (**F**) Representative bright-field images showing a morphological difference in the cell process length of $M\phi^{ACE10}$ versus $M\phi^{WT}$ with measurements of elongation (red lines). (**G**) Quantitative analysis of elongation factor [ratio between total cell length and soma width (*left*) and percentage cell elongation (*right*) in unstimulated $M\phi^{WT}$ versus $M\phi^{ACE10}$]. (**H**) Elongation factor in $M\phi^{WT}$ versus $M\phi^{ACE10}$ stimulated with fibril amyloid-β_{42} for 0, 5, and 30 min. (**I**–**L**) Quantitative MSD protein assay of unstimulated (–) and stimulated with fibril amyloid-β_{42} [100 nM for 24 h (+)] $M\phi^{WT}$ versus $M\phi^{ACE10}$ for the following cytokines: (**I**) TNFα, (**J**) IL6, (**K**) CXCL1, and (**L**) IL1β. (**M**) Quantitative analysis of a cell viability MTT assay in $M\phi^{WT}$ versus $M\phi^{ACE10}$ after 24 h of exposure to 1 μM fibril amyloid-β_{42} (n = 3 mice/genotype group, n = 6 wells/group; one-tailed Student t-test). Data from individual mouse, group mean ± SEM as well as fold increase and percentage decrease and increase between groups are shown. $^{*}P < 0.05$, $^{**}P < 0.01$, $^{***}P < 0.001$, $^{****}P < 0.0001$. ns = non-significant, by two-way or one-way ANOVA and Bonferroni's post-test, while asterisks in parentheses signify a two-group comparison using the unpaired two-tailed Student t-test.

inflammatory, pro-healing phenotype (McWhorter *et al.*, 2013; Rentsendorj *et al.*, 2018).

Along this line, the immune profiles of ACE^{10} and wild-type macrophages were further analysed using a highly sensitive MSD multiplex inflammatory assay. The results are in good accordance with the results obtained *in vivo* (Fig. 1M and N) and show that stimulation of both wild-type and ACE^{10} macrophages with fibril amyloid-β_{42} for 24 h increased expression of TNFα (Fig. 5I; $P < 0.0001$). However, the magnitude of TNFα increase was significantly lower in the ACE^{10} macrophages (Fig. 5I; $P < 0.001$). While IL-6, CXCL1, and IL-1β concentrations were also elevated in both wild-type and ACE^{10} macrophages in response to fibril amyloid-β_{42} stimulation, the degree of increase was more reserved in the ACE^{10} macrophages than in the wild-type cells (Fig. 5J–L and Supplementary Fig. 5C–F). Therefore, this assay showed that the expression of pro-inflammatory cytokines is generally reduced in ACE^{10} relative to wild-type macrophages when equivalently stimulated with amyloid-β. Finally, we examined the viability of wild-type versus ACE^{10} macrophages following a 24-h exposure to higher concentration of fibril amyloid-β_{42} (1 μM). In this assay, on average 50% of ACE^{10} macrophages appeared to survive, compared to only ~30% of the wild-type macrophages (Fig. 5M; $P < 0.05$).

Discussion

Peripheral monocyte migration into the CNS, the role of ACE, and their possible contribution in resisting

Alzheimer's-associated neuropathology and cognitive decline are subjects of intense investigation and controversy (Ajami *et al.*, 2007; Butovsky *et al.*, 2007; El Khoury *et al.*, 2007; Mildner *et al.*, 2007; Lebson *et al.*, 2010; Bernstein *et al.*, 2014*b*; Koronyo *et al.*, 2015). In this study, we addressed these fundamental questions and demonstrated: (i) in a partial bone marrow transplantation paradigm with head shielding (protecting the brain from irradiation), there was a measurable migration of peripheral monocytes into the retina and brain parenchyma of AD^+ mice. While low in number, these cells critically localized around amyloid-β plaques and reduced cerebral amyloid-β burden and inflammation; (ii) engrafted ACE^{10} monocytes in the brains of AD^+ mice are found at about three times higher numbers than wild-type cells and are more effective in restricting neuropathology; (iii) compared to wild-type macrophages, ACE^{10} cells in AD^+ mouse brains express ~60% lower levels of TNFα and 3.2-fold higher IGF1, associated with restricting neurodegeneration and cognitive deficits; (iv) non-invasive retinal imaging demonstrates the feasibility of tracking the movements of GFP^+-monocytes into the retina of AD^+ mice in real time; (v) adoptive transfer of $CD115^+$ ACE^{10} monocytes into the peripheral blood of symptomatic AD^+ mice, an irradiation-free translational approach, is highly effective in reducing vascular amyloidosis and preserving synapses and cognitive function; (vi) ACE^{10} macrophages exhibit strikingly unique immunological profiles, with enhanced surface receptors and augmented ability to bind, internalize, degrade, and destroy fibrillar, prion rod-like, and soluble oligomeric amyloid-β_{42} species; and (vii) the elongated cell morphology and molecular signature of ACE^{10} macrophages suggest an anti-inflammatory, pro-healing, and highly resilient phenotype that may help fight against Alzheimer's disease.

Although several studies have demonstrated the ability of human blood mononuclear cells, monocytes and macrophages, to phagocytose fibrillar amyloid-β and remove plaques from the brains of Alzheimer's disease model mice (Malm *et al.*, 2005; Simard *et al.*, 2006; Butovsky *et al.*, 2007; Fiala *et al.*, 2007; Lai and McLaurin, 2012; Koronyo *et al.*, 2015), their direct involvement in the clearance of non-fibrillar forms of amyloid-β and possible neuroprotection in Alzheimer's disease is still highly debated (Fiala *et al.*, 2005; Mildner *et al.*, 2007). Moreover, previous studies did not measure the degree of clearance of defined and stabilized amyloid-β_{42} structures associated with Alzheimer's disease neuropathology such as prion rod-like assemblies or soluble oligomers. While amyloid-β plaque burden in the brain appears very limited in predicting cognitive decline (Jansen *et al.*, 2018) and may even serve as a mediator of an effective innate immune response against foreign pathogens (Soscia *et al.*, 2010), soluble amyloid-β_{42} oligomers and prion rod-like structures have been shown to be highly neurotoxic and more elusive to phagocytic immune cells (Selkoe, 2008; Shankar *et al.*, 2008). Because of the meta-stability of these amyloid-β_{42} assemblies, structure-activity determinations with respect to macrophage responses have been problematic. Here, using structurally stabilized oligomers and well-characterized prion rod-like and fibrillar amyloid-β_{42}, we were able to accomplish these determinations with respect to binding efficacy, internalization, and degradation by wild-type and ACE^{10} macrophages. Our studies show that in the wild-type cells, oligomers of amyloid-β_{42} are found in very low amounts in endosomes and lysosomes, the cellular ubiquitin/proteasome machinery that degrades misfolded proteins (Majumdar *et al.*, 2008). Yet, ACE overexpression and enzymatic function significantly shifted macrophage behaviour and their ability to also target amyloid-β_{42} oligomers to endosomes (up to 40 times higher as compared to those found in wild-type macrophages; Fig. 4C–H). As a result of the subcellular localization of amyloid-β_{42} in ACE^{10} macrophages and the increased levels of amyloid-β-degrading enzymes (i.e. ACE, MMP9), the net concentrations of amyloid-β_{42} remaining after a 24-h incubation with ACE^{10} versus wild-type macrophages were as much as 80% lower.

The unique morphological and immunological profiles of ACE^{10} macrophages in response to amyloid-β_{42} were assessed using various techniques. One mechanism that could explain this superior performance is increased surface expression of scavenger receptors, including Scara1, TREM2, CD163, and especially CD36, all of which have been previously shown to facilitate amyloid-β internalization and clearance by myelomonocytic cells (Koronyo *et al.*, 2015; Rentsendorj *et al.*, 2018). In particular, Scara1 expression was tightly associated with the extent of phagocytosis of amyloid-β_{42} fibrils, but less so for prion rod-like structures and soluble oligomers. In the ACE^{10} macrophages, CD36 expression was drastically elevated (increased 6- to 36-fold) and tightly associated with increased uptake of all three types of amyloid-β assemblies. In contrast, the wild-type macrophages displayed no association between surface CD36 expression and uptake of amyloid-β_{42} fibrils and oligomers, though a strong correlation was observed with rod-like structures. The reason for this phenomenon is currently unknown. Future studies are needed to better understand the molecular immune mechanisms at play to remove pathogenic forms of amyloid-β. Further *in vitro* techniques supported the enhanced molecular characteristics of the ACE^{10} macrophages, before and after exposure to amyloid-β_{42} conformers. All assay findings consistently suggested that these bone marrow-derived cells exhibit an anti-inflammatory (i.e. low TNFα and iNOS, high IGF1, arginase-1, and MMP9) and a pro-healing/protective (i.e. elongated cell morphology) phenotype. These effects were dependent on ACE enzymatic activity and were eliminated when treating the cells with ACE inhibitors. In contrast, previous studies demonstrated that peritoneal-derived ACE^{10} macrophages, under conditions of acute foreign invasion or cancer models, enhanced their effective immune reactivity in the periphery to resolve disease while exhibiting a highly pro-inflammatory profile (Bernstein *et al.*, 2018). These diverse phenotypes of the ACE^{10} cells may

suggest their ability to promptly and effectively respond to insults in a tissue- and disease-specific manner. This variation in response could also be due to the different stages of healing for which these cells are recruited (i.e. chronic inflammation versus acute injury); nonetheless, their remedial capacity is strongly evident. The enhanced immune response of ACE^{10} macrophages to acute infection or tumour has repeatedly been shown to not be dependent on the production of angiotensin II or any angiotensin peptide by ACE (reviewed in Bernstein *et al.*, 2018). While this was not formally tested in our study, we believe it most likely that the unique phenotype of the ACE^{10} macrophages here are probably also due to other mechanisms besides angiotensin II. We further note a recent study documenting that ACE cleaves dozens, if not hundreds, of different peptide substrates (Semis *et al.*, 2019).

Our *in vivo* studies assessed the exclusive contribution of peripherally derived ACE^{10} monocytes and macrophages in attenuating neuropathology and cognitive deficits in murine models of Alzheimer's disease. Mounting evidence suggests a protective role for innate immune cells in the CNS (El Khoury *et al.*, 2007; Koronyo-Hamaoui *et al.*, 2009; Shechter *et al.*, 2009; Lebson *et al.*, 2010; Bernstein *et al.*, 2014*b*; Koronyo *et al.*, 2015), though some studies have failed to show migration of these cells under neurodegenerative conditions (Mildner *et al.*, 2007), or showed monocyte migration to CNS without effects on behaviour and cerebral amyloid-β levels (Prokop *et al.*, 2015; Varvel *et al.*, 2015; Cronk *et al.*, 2018). Our group previously demonstrated that peripherally derived GFP-labelled monocytes are naturally recruited to brains of Alzheimer's disease model mice (Butovsky *et al.*, 2006, 2007; Koronyo-Hamaoui *et al.*, 2009; Bernstein *et al.*, 2014*b*) and that they directly reduce neuropathology and preserve cognition (Koronyo *et al.*, 2015). This irradiation- and pharmacologically-free approach substantially enriched the $CD115^+$ bone marrow-derived inflammatory monocyte subset in the peripheral blood of AD^+ mice, resulting in spontaneous recruitment of these cells to the CNS, and led to diminished soluble and insoluble amyloid-$\beta_{40,42}$ levels and astrocytosis as well as increased post-synaptic density and preservation of learning and memory (Koronyo *et al.*, 2015; Rentsendorj *et al.*, 2018). When targeting ACE overexpression in macrophages, our earlier studies reported major therapeutic effects in protecting against melanoma and microbial infections (Bernstein *et al.*, 2014*a*, 2018). Our current investigation also strongly suggests neuroprotective effects of ACE^{10} macrophages in Alzheimer's disease mouse models. In accordance, administration of the ACE inhibitor captopril to Alzheimer's disease mice was reported to increase cerebral amyloid-β deposition (Zou *et al.*, 2007). Here, ACE-overexpressing macrophages were consistently potent in clearing amyloid-β_{42} conformers—even the most elusive non-fibrillar forms—and successfully migrated into the mouse brain and retina with an enhanced ability to inhibit pathogenesis. While it appears that ACE overexpression in both the resident microglia and peripheral myelomonocytes work synergistically to restrict Alzheimer's disease-associated pathology and improve cognition in animal models (Bernstein *et al.*, 2014*b*; Koronyo-Hamaoui *et al.*, 2014), the extent of the effect by peripheral ACE^{10} macrophages alone was nonetheless substantial, especially with regards to cerebral vascular amyloidosis. Because of growing reports on the key role of vascular abnormalities in Alzheimer's-related cognitive decline (Ellis *et al.*, 1996; Wyss-Coray *et al.*, 2001; Herzig *et al.*, 2006; Rentsendorj *et al.*, 2018; Nation *et al.*, 2019), the beneficial effects of ACE^{10} macrophages on reducing vascular amyloidosis (CAA severity score) and $GFAP^+$ astroglial reactivation may indicate protection to the neurovascular unit and could explain synaptic and cognitive preservation seen in these mice. Similarly, previous studies in murine Alzheimer's disease models showed that blood infusion with either wild-type or neprilysin-enriched monocytes mitigated neuropathology and cognitive deficits (Lebson *et al.*, 2010; Koronyo *et al.*, 2015) and monocyte depletion exacerbated amyloid-β-plaque pathology (Butovsky *et al.*, 2007; El Khoury *et al.*, 2007).

Specifically, we have shown by two *in vivo* approaches that ACE-overexpressing monocytes are more effective in ameliorating Alzheimer's disease-like pathology and preserving cognition in symptomatic murine models of Alzheimer's disease. Our data showed that even partial bone marrow replacement with ACE^{10} cells (after partial-body irradiation, which avoids the skull area to prevent damage to the blood–brain barrier) leads to a substantial 3-fold increase of ACE^{10} monocytes in the brain, significantly decreasing cerebral amyloid-β plaques, amyloid-β's soluble forms, and astrocytosis. Increased *in vivo* recruitment of ACE^{10} macrophages could be, at least in part, attributed to enhanced secretion of MMP9, an enzyme known to facilitate transmigration of immune cells through the blood–brain barrier (Chaturvedi and Kaczmarek, 2014). These brain-engrafted cells also exhibited ~60% lower TNFα levels and 3.2-fold higher IGF1, adding a major advantage of this therapeutic approach. TNFα is a key pro-inflammatory cytokine that in excess can induce oxidative stress related to the release of iNOS and reactive oxygen species, which are tightly associated with neurotoxicity and functional decline. Moreover, IGF1 is a brain regenerative, neurogenesis-promoting neurotrophic factor with recently discovered anti-inflammatory functions (Gasparini and Xu, 2003). Cerebral IGF1 in murine models of Alzheimer's disease was shown to be elevated following immunomodulation interventions involving increased brain-infiltrating monocytes/macrophages and cognitive preservation (Butovsky *et al.*, 2006; Koronyo-Hamaoui *et al.*, 2009), and another report has demonstrated its direct involvement in reducing amyloid-β plaque burden (Carro *et al.*, 2002). Such substantial changes in TNFα and IGF1 levels in a chronically inflamed brain by ACE^{10} macrophages could, if translated into humans, potentially alter the course of Alzheimer's disease and critically preserve synapses and cognition. This

hypothesis is supported by our observations from the adoptive transfer studies in which enriching the peripheral blood of symptomatic AD^{+} mice with CD115^{+}-Mo^{ACE10} cells resulted in improved cognitive function (Barnes maze test) and pre- and post-synaptic preservation.

In comparison, our previous studies in murine models of Alzheimer's disease involving life-long replacement of CNS-resident microglia and peripheral monocyte and macrophage populations with the ACE-overexpressing cells resulted in an almost complete elimination of cerebral amyloid-β burden, astrocytosis, and full preservation of cognitive functions, similar to the levels seen in the wild-type mice (Koronyo-Hamaoui *et al.*, 2009; Bernstein *et al.*, 2014*b*, 2018; Rentsendorj *et al.*, 2018). As briefly mentioned above, here partial bone marrow replacement or short-term blood enrichment with ACE^{10} macrophages (once a month for 3 months) in animals that already have Alzheimer's disease-like symptoms limited neuropathology by 30–40% (especially vascular amyloidosis), yet remarkably restored cognitive functions to levels indistinguishable from those found in cognitively normal wild-type mice.

Conclusion and translational implications

Despite considerable progress in understanding the aetiology of Alzheimer's disease, an effective treatment remains elusive. The therapeutic potential evidenced in our studies favours selective increase of ACE (Al Mulhim *et al.*, 2019), a peptidase capable of destroying amyloidogenic peptides and enhancing neuroprotective phenotype, in peripheral inflammatory cells that can migrate into the brain and powerfully support tissue-healing processes and cognition. For the first time, we demonstrate a superior ability of ACE^{10} macrophages to eradicate amyloid-β assemblies, particularly Alzheimer's-associated non-fibrillar, oligomeric amyloid-β structures. The infiltration of these cells to the CNS was further validated through live non-invasive imaging of the retina, providing a feasible method to track immune cell migration during disease progression. Moreover, this study reveals the beneficial roles of CD115^{+} bone marrow-derived monocyte subsets and ACE in resisting Alzheimer's pathology, especially important in light of large-scale human genetic studies identifying ACE and innate immune genes as prominently related to Alzheimer's disease (Kehoe *et al.*, 1999, 2003, 2004; Narain *et al.*, 2000; Elkins *et al.*, 2004; Kolsch *et al.*, 2005; Lehmann *et al.*, 2005; Meng *et al.*, 2006; Jochemsen *et al.*, 2014; de Oliveira *et al.*, 2018; Marioni *et al.*, 2018; Kunkle *et al.*, 2019). Further, the marked reduction of Alzheimer's-associated pathology with targeted ACE expression in inflammatory cells raises a clinically imperative question related to the outcome of life-long use of ACE inhibitors in the large number of patients with heart-related conditions (including high blood pressure), or commonly prescribed anti-inflammatory drugs (i.e. NSAIDs). For example, our results and other published data suggest caution in the use of ACE inhibitors, perhaps prioritizing those that do not penetrate the brain, such as benazepril, enalapril or quinapril (Kehoe *et al.*, 2013). We envision the reported approach to be applicable to humans via isolation of monocytes from bone marrow or circulating blood, manipulation *in vitro* to overexpress ACE, followed by reinfusion of the modified cells to the patient. Future direction will focus on developing the practical and clinical protocols for each of these steps. It could involve the use of genetically modified stem cells or viral vectors to modify the isolated immune cells.

In conclusion, this study may alter the vision of Alzheimer's disease in human health in two ways: increased attention to potential neuropathological consequences of ACE inhibitors and anti-inflammatory drugs, and discovery of a novel Alzheimer's disease immunotherapy to deliver ACE and therapeutic monocytes to the site of Alzheimer's disease pathological manifestation.

Acknowledgements

The authors thank Xiao Z. Shen for his assistance with brain flow cytometry analysis, Ellen Bernstein for help with ACE^{10} transgenic mice, and Dr Mitra Mastali from Dr Jennifer Van Eyk's Protein Quantification Core Laboratory at the Clinical Biosystems Research Institute, Cedars-Sinai Medical Center for assistance with the MSD-ELISA data. We also thank Mia Oviatt and Jo Ann Eliason for help with editing and Samuel Fuchs for his illustration of Supplementary Fig. 1C and help with thumbnail. The authors dedicate the manuscript to the memory of Natalie Radom Bernstein, Lillian Jones Black, and Salomon Moni Hamaoui, who died of Alzheimer's disease.

Funding

Research reported in this publication was supported by the National Institute on Aging of the National Institutes of Health under Awards Number R01 AG055865 (M.K.H.) and R01 AG042195 (D.B.T.), A2013328S00 BrightFocus Foundation Award (M.K.H.), The Coins for Alzheimer's Research Trust – CART Fund (M.K.H.), The Saban Foundation and The Marciano Foundation (M.K.H.).

Competing interests

The authors report no competing interests.

Supplementary material

Supplementary material is available at *Brain* online.

References

Ajami B, Bennett JL, Krieger C, Tetzlaff W, Rossi FM. Local self-renewal can sustain CNS microglia maintenance and function throughout adult life. Nat Neurosci 2007; 10: 1538–43.

Akiyama H, Barger S, Barnum S, Bradt B, Bauer J, Cole GM, et al. Inflammation and Alzheimer's disease. Neurobiol Aging 2000; 21: 383–421.

Al Mulhim NS, Kehoe PG, Miners JS. Divergence in the activity of the N- and C- catalytic domains of ACE1-implications for the role of the renin-angiotensin system in Alzheimer's disease. Acta Neuropathol Commun 2019; 7: 57.

Alzheimer's Association. Alzheimer's disease facts and figures. Alzheimers Dement 2019; 15: 321–87.

Ardura-Fabregat A, Boddeke E, Boza-Serrano A, Brioschi S, Castro-Gomez S, Ceyzeriat K, et al. Targeting neuroinflammation to Treat Alzheimer's disease. CNS Drugs 2017; 31: 1057–82.

Bales KR, Du Y, Holtzman D, Cordell B, Paul SM. Neuroinflammation and Alzheimer's disease: critical roles for cytokine/Abeta-induced glial activation, NF-kappaB, and apolipoprotein E. Neurobiol Aging 2000; 21: 427–32; discussion 51–3.

Bernstein KE, Gonzalez-Villalobos RA, Giani JF, Shah K, Bernstein E, Janjulia T, et al. Angiotensin-converting enzyme overexpression in myelocytes enhances the immune response. Biol Chem 2014a; 395: 1173–8.

Bernstein KE, Khan Z, Giani JF, Cao DY, Bernstein EA, Shen XZ. Angiotensin-converting enzyme in innate and adaptive immunity. Nat Rev Nephrol 2018; 14: 325–36.

Bernstein KE, Koronyo Y, Salumbides BC, Sheyn J, Pelissier L, Lopes DH, et al. Angiotensin-converting enzyme overexpression in myelomonocytes prevents Alzheimer's-like cognitive decline. J Clin Invest 2014b; 124: 1000–12.

Bianchi VE, Locatelli V, Rizzi L. Neurotrophic and neuroregenerative effects of GH/IGF1. Int J Mol Sci 2017; 18: 2441.

Bitan G. Structural study of metastable amyloidogenic protein oligomers by photo-induced cross-linking of unmodified proteins. Methods Enzymol 2006; 413: 217–36.

Bitan G, Kirkitadze MD, Lomakin A, Vollers SS, Benedek GB, Teplow DB. Amyloid beta-protein (Abeta) assembly: abeta 40 and abeta 42 oligomerize through distinct pathways. Proc Natl Acad Sci U S A 2003; 100: 330–5.

Bitan G, Lomakin A, Teplow DB. Amyloid beta-protein oligomerization: prenucleation interactions revealed by photo-induced cross-linking of unmodified proteins. J Biol Chem 2001; 276: 35176–84.

Bitan G, Teplow DB. Rapid photochemical cross-linking: a new tool for studies of metastable, amyloidogenic protein assemblies. Acc Chem Res 2004; 37: 357–64.

Bitan G, Teplow DB. Preparation of aggregate-free, low molecular weight amyloid-beta for assembly and toxicity assays. Methods Mol Biol 2005; 299: 3–9.

Boissonneault V, Filali M, Lessard M, Relton J, Wong G, Rivest S. Powerful beneficial effects of macrophage colony-stimulating factor on beta-amyloid deposition and cognitive impairment in Alzheimer's disease. Brain 2009; 132: 1078–92.

Butovsky O, Koronyo-Hamaoui M, Kunis G, Ophir E, Landa G, Cohen H, et al. Glatiramer acetate fights against Alzheimer's disease by inducing dendritic-like microglia expressing insulin-like growth factor 1. Proc Natl Acad Sci U S A 2006; 103: 11784–9.

Butovsky O, Kunis G, Koronyo-Hamaoui M, Schwartz M. Selective ablation of bone marrow-derived dendritic cells increases amyloid plaques in a mouse Alzheimer's disease model. Eur J Neurosci 2007; 26: 413–6.

Cao W, Zheng H. Peripheral immune system in aging and Alzheimer's disease. Mol Neurodegener 2018; 13: 51.

Carro E, Trejo JL, Gomez-Isla T, LeRoith D, Torres-Aleman I. Serum insulin-like growth factor I regulates brain amyloid-beta levels. Nat Med 2002; 8: 1390–7.

Chaturvedi M, Kaczmarek L. Mmp-9 inhibition: a therapeutic strategy in ischemic stroke. Mol Neurobiol 2014; 49: 563–73.

Colton CA, Chernyshev ON, Gilbert DL, Vitek MP. Microglial contribution to oxidative stress in Alzheimer's disease. Ann N Y Acad Sci 2000; 899: 292–307.

Cronk JC, Filiano AJ, Louveau A, Marin I, Marsh R, Ji E, et al. Peripherally derived macrophages can engraft the brain independent of irradiation and maintain an identity distinct from microglia. J Exp Med 2018; 215: 1627–47.

Da Mesquita S, Louveau A, Vaccari A, Smirnov I, Cornelison RC, Kingsmore KM, et al. Functional aspects of meningeal lymphatics in ageing and Alzheimer's disease. Nature 2018; 560: 185–91.

de Oliveira FF, Chen ES, Smith MC, Bertolucci PHF. Pharmacogenetics of angiotensin-converting enzyme inhibitors in patients with Alzheimer's disease dementia. Curr Alzheimer Res 2018; 15: 386–98.

El Khoury J, Toft M, Hickman SE, Means TK, Terada K, Geula C, et al. Ccr2 deficiency impairs microglial accumulation and accelerates progression of Alzheimer-like disease. Nat Med 2007; 13: 432–8.

Elkins JS, Douglas VC, Johnston SC. Alzheimer disease risk and genetic variation in ACE: a meta-analysis. Neurology 2004; 62: 363–8.

Ellis RJ, Olichney JM, Thal LJ, Mirra SS, Morris JC, Beekly D, et al. Cerebral amyloid angiopathy in the brains of patients with Alzheimer's disease: the CERAD experience, Part XV. Neurology 1996; 46: 1592–6.

Fiala M, Cribbs DH, Rosenthal M, Bernard G. Phagocytosis of amyloid-beta and inflammation: two faces of innate immunity in Alzheimer's disease. J Alzheimer's Dis: JAD 2007; 11: 457–63.

Fiala M, Lin J, Ringman J, Kermani-Arab V, Tsao G, Patel A, et al. Ineffective phagocytosis of amyloid-beta by macrophages of Alzheimer's disease patients. J Alzheimer's Dis: JAD 2005; 7: 221–32; discussion 55–62.

Fradinger EA, Lazo ND, Teplow DB. Studying amyloid β-protein assembly. In: Xia W, editor. Amyloid precursor protein: a practical approach. Boca Raton, FL: CRC Press Inc.; 2005. p. 83–110.

Frenkel D, Wilkinson K, Zhao L, Hickman SE, Means TK, Puckett L, et al. Scara1 deficiency impairs clearance of soluble amyloid-beta by mononuclear phagocytes and accelerates Alzheimer's-like disease progression. Nat Commun 2013; 4: 2030.

Gasparini L, Xu H. Potential roles of insulin and IGF-1 in Alzheimer's disease. Trends Neurosci 2003; 26: 404–6.

Gjoneska E, Pfenning AR, Mathys H, Quon G, Kundaje A, Tsai LH, et al. Conserved epigenomic signals in mice and humans reveal immune basis of Alzheimer's disease. Nature 2015; 518: 365–9.

Glabe CC. Amyloid accumulation and pathogensis of Alzheimer's disease: significance of monomeric, oligomeric and fibrillar Abeta. Subcell Biochem 2005; 38: 167–77.

Haass C, Selkoe DJ. Soluble protein oligomers in neurodegeneration: lessons from the Alzheimer's amyloid beta-peptide. Nat Rev Mol Cell Biol 2007; 8: 101–12.

Han CZ, Juncadella IJ, Kinchen JM, Buckley MW, Klibanov AL, Dryden K, et al. Macrophages redirect phagocytosis by non-professional phagocytes and influence inflammation. Nature 2016; 539: 570–4.

Hayden EY, Teplow DB. Continuous flow reactor for the production of stable amyloid protein oligomers. Biochemistry 2012; 51: 6342–9.

Hemming ML, Selkoe DJ. Amyloid beta-protein is degraded by cellular angiotensin-converting enzyme (ACE) and elevated by an ACE inhibitor. J Biol Chem 2005; 280: 37644–50.

Heneka MT, Carson MJ, El Khoury J, Landreth GE, Brosseron F, Feinstein DL, et al. Neuroinflammation in Alzheimer's disease. Lancet Neurol 2015; 14: 388–405.

Herzig MC, Van Nostrand WE, Jucker M. Mechanism of cerebral beta-amyloid angiopathy: murine and cellular models. Brain Pathol 2006; 16: 40–54.

Hickman SE, Allison EK, El Khoury J. Microglial dysfunction and defective beta-amyloid clearance pathways in aging Alzheimer's disease mice. J Neurosci 2008; 28: 8354–60.

Hong S, Beja-Glasser VF, Nfonoyim BM, Frouin A, Li S, Ramakrishnan S, et al. Complement and microglia mediate early synapse loss in Alzheimer mouse models. Science 2016; 352: 712–6.

Jack CR, Jr., Bennett DA, Blennow K, Carrillo MC, Dunn B, Haeberlein SB, et al. NIA-AA research framework: toward a biological definition of Alzheimer's disease. Alzheimers Dement 2018; 14: 535–62.

Jansen WJ, Ossenkoppele R, Tijms BM, Fagan AM, Hansson O, Klunk WE, et al. Association of cerebral amyloid-beta aggregation with cognitive functioning in persons without dementia. JAMA Psychiatry 2018; 75: 84–95.

Jay T, Lamb B, Landreth G. Peripheral macrophages not ADept at amyloid clearance. J Exp Med 2015a; 212: 1758.

Jay TR, Miller CM, Cheng PJ, Graham LC, Bemiller S, Broihier ML, et al. TREM2 deficiency eliminates TREM2+ inflammatory macrophages and ameliorates pathology in Alzheimer's disease mouse models. J Exp Med 2015b; 212: 287–95.

Jochemsen HM, Teunissen CE, Ashby EL, van der Flier WM, Jones RE, Geerlings MI, et al. The association of angiotensin-converting enzyme with biomarkers for Alzheimer's disease. Alzheimers Res Ther 2014; 6: 27.

Johnson MB, Stevens B. Pruning hypothesis comes of age. Nature 2018; 554: 438–9.

Kehoe PG, Davies NM, Martin RM, Ben-Shlomo Y. Associations of angiotensin targeting antihypertensive drugs with mortality and hospitalization in primary care patients with dementia. J Alzheimer's Dis: JAD 2013; 33: 999–1008.

Kehoe PG, Katzov H, Andreasen N, Gatz M, Wilcock GK, Cairns NJ, et al. Common variants of ACE contribute to variable age-at-onset of Alzheimer's disease. Hum Genet 2004; 114: 478–83.

Kehoe PG, Katzov H, Feuk L, Bennet AM, Johansson B, Wiman B, et al. Haplotypes extending across ACE are associated with Alzheimer's disease. Hum Mol Genet 2003; 12: 859–67.

Kehoe PG, Miners S, Love S. Angiotensins in Alzheimer's disease-friend or foe? Trends Neurosci 2009; 32: 619–28.

Kehoe PG, Russ C, McIlory S, Williams H, Holmans P, Holmes C, et al. Variation in DCP1, encoding ACE, is associated with susceptibility to Alzheimer disease. Nat Genet 1999; 21: 71–2.

Keren-Shaul H, Spinrad A, Weiner A, Matcovitch-Natan O, Dvir-Szternfeld R, Ulland TK, et al. A unique microglia type associated with restricting development of Alzheimer's disease. Cell 2017; 169: 1276–90 e17.

Kim SM, Mun BR, Lee SJ, Joh Y, Lee HY, Ji KY, et al. TREM2 promotes Abeta phagocytosis by upregulating C/EBPalpha-dependent CD36 expression in microglia. Sci Rep 2017; 7: 11118.

Kirkitadze MD, Kowalska A. Molecular mechanisms initiating amyloid beta-fibril formation in Alzheimer's disease. Acta Biochim Pol 2005; 52: 417–23.

Kolsch H, Jessen F, Freymann N, Kreis M, Hentschel F, Maier W, et al. ACE I/D polymorphism is a risk factor of Alzheimer's disease but not of vascular dementia. Neurosci Lett 2005; 377: 37–9.

Koronyo Y, Biggs D, Barron E, Boyer DS, Pearlman JA, Au WJ, et al. Retinal amyloid pathology and proof-of-concept imaging trial in Alzheimer's disease. JCI Insight 2017; 2: e93621.

Koronyo-Hamaoui M, Ko MK, Koronyo Y, Azoulay D, Seksenyan A, Kunis G, et al. Attenuation of AD-like neuropathology by harnessing peripheral immune cells: local elevation of IL-10 and MMP-9. J Neurochem 2009; 111: 1409–24.

Koronyo-Hamaoui M, Koronyo Y, Ljubimov AV, Miller CA, Ko MK, Black KL, et al. Identification of amyloid plaques in retinas from Alzheimer's patients and noninvasive in vivo optical imaging of retinal plaques in a mouse model. Neuroimage 2011; 54: S204–17.

Koronyo-Hamaoui M, Shah K, Koronyo Y, Bernstein E, Giani JF, Janjulia T, et al. ACE overexpression in myelomonocytic cells: effect on a mouse model of Alzheimer's disease. Curr Hypertens Rep 2014; 16: 444.

Koronyo Y, Salumbides BC, Black KL, Koronyo-Hamaoui M. Alzheimer's disease in the retina: imaging retinal abeta plaques for early diagnosis and therapy assessment. Neurodegener Dis 2012; 10: 285–93.

Koronyo Y, Salumbides BC, Sheyn J, Pelissier L, Li S, Ljubimov V, et al. Therapeutic effects of glatiramer acetate and grafted CD115(+) monocytes in a mouse model of Alzheimer's disease. Brain 2015; 138: 2399–422.

Krasemann S, Madore C, Cialic R, Baufeld C, Calcagno N, El Fatimy R, et al. The TREM2-APOE pathway drives the transcriptional phenotype of dysfunctional microglia in neurodegenerative diseases. Immunity 2017; 47: 566–81.e9.

Kunkle BW, Grenier-Boley B, Sims R, Bis JC, Damotte V, Naj AC, et al. Genetic meta-analysis of diagnosed Alzheimer's disease identifies new risk loci and implicates Abeta, tau, immunity and lipid processing. Nat Genet 2019; 51: 414–30.

La Morgia C, Ross-Cisneros FN, Koronyo Y, Hannibal J, Gallassi R, Cantalupo G, et al. Melanopsin retinal ganglion cell loss in Alzheimer disease. Ann Neurol 2016; 79: 90–109.

Lai AY, McLaurin J. Clearance of amyloid-beta peptides by microglia and macrophages: the issue of what, when and where. Future Neurol 2012; 7: 165–76.

Lebson L, Nash K, Kamath S, Herber D, Carty N, Lee DC, et al. Trafficking CD11b-positive blood cells deliver therapeutic genes to the brain of amyloid-depositing transgenic mice. J Neurosci 2010; 30: 9651–8.

Lehmann DJ, Cortina-Borja M, Warden DR, Smith AD, Sleegers K, Prince JA, et al. Large meta-analysis establishes the ACE insertion-deletion polymorphism as a marker of Alzheimer's disease. Am J Epidemiol 2005; 162: 305–17.

Lopes DH, Sinha S, Rosensweig C, Bitan G. Application of photochemical cross-linking to the study of oligomerization of amyloidogenic proteins. Methods Mol Biol 2012; 849: 11–21.

Majumdar A, Chung H, Dolios G, Wang R, Asamoah N, Lobel P, et al. Degradation of fibrillar forms of Alzheimer's amyloid beta-peptide by macrophages. Neurobiol Aging 2008; 29: 707–15.

Malm TM, Koistinaho M, Parepalo M, Vatanen T, Ooka A, Karlsson S, et al. Bone-marrow-derived cells contribute to the recruitment of microglial cells in response to beta-amyloid deposition in APP/PS1 double transgenic Alzheimer mice. Neurobiol Dis 2005; 18: 134–42.

Marioni RE, Harris SE, Zhang Q, McRae AF, Hagenaars SP, Hill WD, et al. GWAS on family history of Alzheimer's disease. Transl Psychiatry 2018; 8: 99.

Masters CL, Bateman R, Blennow K, Rowe CC, Sperling RA, Cummings JL. Alzheimer's disease. Nat Rev Dis Primers 2015; 1: 15056.

McGeer PL, McGeer EG. Local neuroinflammation and the progression of Alzheimer's disease. J Neurovirol 2002; 8: 529–38.

McWhorter FY, Wang T, Nguyen P, Chung T, Liu WF. Modulation of macrophage phenotype by cell shape. Proc Natl Acad Sci U S A 2013; 110: 17253–8.

Meng Y, Baldwin CT, Bowirrat A, Waraska K, Inzelberg R, Friedland RP, et al. Association of polymorphisms in the Angiotensin-converting enzyme gene with Alzheimer disease in an Israeli Arab community. Am J Hum Genet 2006; 78: 871–7.

Michaud JP, Bellavance MA, Prefontaine P, Rivest S. Real-time in vivo imaging reveals the ability of monocytes to clear vascular amyloid beta. Cell Rep 2013; 5: 646–53.

Mildner A, Schmidt H, Nitsche M, Merkler D, Hanisch UK, Mack M, et al. Microglia in the adult brain arise from Ly-6ChiCCR2+ monocytes only under defined host conditions. Nat Neurosci 2007; 10: 1544–53.

Miners S, Ashby E, Baig S, Harrison R, Tayler H, Speedy E, et al. Angiotensin-converting enzyme levels and activity in Alzheimer's disease: differences in brain and CSF ACE and association with ACE1 genotypes. Am J Transl Res 2009; 1: 163–77.

Miners JS, Ashby E, Van Helmond Z, Chalmers KA, Palmer LE, Love S, et al. Angiotensin-converting enzyme (ACE) levels and activity in Alzheimer's disease, and relationship of perivascular ACE-1 to cerebral amyloid angiopathy. Neuropathol Appl Neurobiol 2008; 34: 181–93.

Morgan D, Gordon MN, Tan J, Wilcock D, Rojiani AM. Dynamic complexity of the microglial activation response in transgenic models of amyloid deposition: implications for Alzheimer therapeutics. J Neuropathol Exp Neurol 2005; 64: 743–53.

Narain Y, Yip A, Murphy T, Brayne C, Easton D, Evans JG, et al. The ACE gene and Alzheimer's disease susceptibility. J Med Genet 2000; 37: 695–7.

Nation DA, Sweeney MD, Montagne A, Sagare AP, D'Orazio LM, Pachicano M. Blood-brain barrier breakdown is an early biomarker of human cognitive dysfunction. Nat Med 2019; 25: 270–6.

Okabe M, Ikawa M, Kominami K, Nakanishi T, Nishimune Y. 'Green mice' as a source of ubiquitous green cells. FEBS Lett 1997; 407: 313–9.

Okwan-Duodu D, Datta V, Shen XZ, Goodridge HS, Bernstein EA, Fuchs S, et al. Angiotensin-converting enzyme overexpression in mouse myelomonocytic cells augments resistance to Listeria and methicillin-resistant Staphylococcus aureus. J Biol Chem 2010; 285: 39051–60.

Pey P, Pearce RK, Kalaitzakis ME, Griffin WS, Gentleman SM. Phenotypic profile of alternative activation marker CD163 is different in Alzheimer's and Parkinson's disease. Acta Neuropathol Commun 2014; 2: 21.

Prinz M, Priller J, Sisodia SS, Ransohoff RM. Heterogeneity of CNS myeloid cells and their roles in neurodegeneration. Nat Neurosci 2011; 14: 1227–35.

Prokop S, Miller KR, Drost N, Handrick S, Mathur V, Luo J, et al. Impact of peripheral myeloid cells on amyloid-beta pathology in Alzheimer's disease-like mice. J Exp Med 2015; 212: 1811–8.

Rentsendorj A, Sheyn J, Fuchs DT, Daley D, Salumbides BC, Schubloom HE, et al. A novel role for osteopontin in macrophage-mediated amyloid-beta clearance in Alzheimer's models. Brain Behav Immun 2018; 67: 163–80.

Roussos P, Katsel P, Fam P, Tan W, Purohit DP, Haroutunian V. The triggering receptor expressed on myeloid cells 2 (TREM2) is associated with enhanced inflammation, neuropathological lesions and increased risk for Alzheimer's dementia. Alzheimers Dement 2015; 11: 1163–70.

Selkoe DJ. Soluble oligomers of the amyloid beta-protein impair synaptic plasticity and behavior. Behav Brain Res 2008; 192: 106–13.

Semis M, Gugiu GB, Bernstein EA, Bernstein KE, Kalkum M. The plethora of angiotensin-converting enzyme-processed peptides in mouse plasma. Anal Chem 2019; 91: 6440–53.

Shankar GM, Li S, Mehta TH, Garcia-Munoz A, Shepardson NE, Smith I, et al. Amyloid-beta protein dimers isolated directly from Alzheimer's brains impair synaptic plasticity and memory. Nat Med 2008; 14: 837–42.

Shechter R, London A, Varol C, Raposo C, Cusimano M, Yovel G, et al. Infiltrating blood-derived macrophages are vital cells playing an anti-inflammatory role in recovery from spinal cord injury in mice. PLoS Med 2009; 6: e1000113.

Shen XZ, Li P, Weiss D, Fuchs S, Xiao HD, Adams JA, et al. Mice with enhanced macrophage angiotensin-converting enzyme are resistant to melanoma. Am J Pathol 2007; 170: 2122–34.

Simard AR, Soulet D, Gowing G, Julien JP, Rivest S. Bone marrow-derived microglia play a critical role in restricting senile plaque formation in Alzheimer's disease. Neuron 2006; 49: 489–502.

Soscia SJ, Kirby JE, Washicosky KJ, Tucker SM, Ingelsson M, Hyman B, et al. The Alzheimer's disease-associated amyloid beta-protein is an antimicrobial peptide. PLoS One 2010; 5: e9505.

Spadaro O, Camell CD, Bosurgi L, Nguyen KY, Youm YH, Rothlin CV, et al. IGF1 Shapes Macrophage Activation in Response to Immunometabolic Challenge. Cell Rep 2017; 19: 225–34.

Town T, Laouar Y, Pittenger C, Mori T, Szekely CA, Tan J, et al. Blocking TGF-beta-Smad2/3 innate immune signaling mitigates Alzheimer-like pathology. Nat Med 2008; 14: 681–7.

Valero J, Bernardino L, Cardoso FL, Silva AP, Fontes-Ribeiro C, Ambrosio AF, et al. Impact of neuroinflammation on hippocampal neurogenesis: relevance to aging and Alzheimer's disease. J Alzheimer's Dis: JAD 2017; 60: S161–8.

Vannella KM, Wynn TA. Mechanisms of organ injury and repair by macrophages. Annu Rev Physiol 2017; 79: 593–617.

Varvel NH, Grathwohl SA, Degenhardt K, Resch C, Bosch A, Jucker M, et al. Replacement of brain-resident myeloid cells does not alter cerebral amyloid-beta deposition in mouse models of Alzheimer's disease. J Exp Med 2015; 212: 1803–9.

Viola KL, Klein WL. Amyloid beta oligomers in Alzheimer's disease pathogenesis, treatment, and diagnosis. Acta Neuropathol 2015; 129: 183–206.

Walsh DM, Lomakin A, Benedek GB, Condron MM, Teplow DB. Amyloid beta-protein fibrillogenesis. Detection of a protofibrillar intermediate. J Biol Chem 1997; 272: 22364–72.

Walsh DM, Selkoe DJ. Deciphering the molecular basis of memory failure in Alzheimer's disease. Neuron 2004; 44: 181–93.

Wyss-Coray T. Inflammation in Alzheimer disease: driving force, bystander or beneficial response? Nat Med 2006; 12: 1005–15.

Wyss-Coray T, Lin C, Yan F, Yu GQ, Rohde M, McConlogue L, et al. TGF-beta1 promotes microglial amyloid-beta clearance and reduces plaque burden in transgenic mice. Nat Med 2001; 7: 612–8.

Yamanaka M, Ishikawa T, Griep A, Axt D, Kummer MP, Heneka MT. PPARgamma/RXRalpha-induced and CD36-mediated microglial amyloid-beta phagocytosis results in cognitive improvement in amyloid precursor protein/presenilin 1 mice. J Neurosci 2012; 32: 17321–31.

Yin Z, Raj D, Saiepour N, Van Dam D, Brouwer N, Holtman IR, et al. Immune hyperreactivity of Aβ plaque-associated microglia in Alzheimer's disease. Neurobiol Aging 2017; 55: 115–22.

Zou K, Yamaguchi H, Akatsu H, Sakamoto T, Ko M, Mizoguchi K, et al. Angiotensin-converting enzyme converts amyloid beta-protein 1-42 (Abeta(1-42)) to Abeta(1-40), and its inhibition enhances brain Abeta deposition. J Neurosci 2007; 27: 8628–35.

Zuroff L, Daley D, Black KL, Koronyo-Hamaoui M. Clearance of cerebral Abeta in Alzheimer's disease: reassessing the role of microglia and monocytes. Cell Mol Life Sci 2017; 74: 2167–201.